Title: Soil Productivity, Efficiency and Resilience Emerge from Self-Organizing Processes Mediated by Management.

Authors: Andrew L. Neal[1*], Aurélie Bacq-Labreuil[2], Xiaoxian Zhang[1], Kevin Coleman[1], Sacha J. Mooney[2], Karl Ritz[2], John W. Crawford[1]

Affiliations:

[1]Department of Sustainable Agriculture Sciences, Rothamsted Research, Harpenden, AL5 2JQ, United Kingdom.

[2]Division of Agriculture and Environmental Science, School of Biosciences, The University of Nottingham, Sutton Bonington Campus, LE12 5RD, United Kingdom.

*Correspondence to: andy.neal@rothamsted.ac.uk (ALN).

Abstract: Soil is a nexus of risks associated with meeting future food demands in the face of dwindling water resources, climate uncertainty and biodiversity collapse. Thus, soil interventions have the potential to simultaneously mitigate (or exacerbate) them all. We integrate metagenomic, physical and mathematical analyses to show how the capacity of soil to support net primary productivity is linked to metabolic efficiency and resilience of these properties to perturbations in water and nutrient inputs. The proposed mechanisms and observed temporal behavior predict that synergistic risk mitigation is limited by cumulative rates of carbon metabolism, and that soil carbon sequestration is a *consequence* rather than a *driver* of change. The results highlight fundamental constraints and new opportunities to achieve food security and manage the land-climate interface.

Introduction

The recent IPCC report on Land Use and Climate Change[1] highlights the fundamental importance of ensuring future land-use strategies account for coupling between soil and climate. Although organic carbon (OC) is known to play a critical role, we do not understand the mechanisms adequately, limiting our ability to manage that coupling. In particular, we do not know why OC changes the dynamics of the soil system to affect the capacity of soil to support net primary productivity (NPP).

The complex micro-structure of soil (*i.e.* structural features of the pore network smaller than 100 μm) allows co-existence of air and water across a wide range of environmental conditions and determines the rate and nature of resident microbial processes[2]. The resultant fractal-like air: water interface maximises the area of the boundary between atmosphere and land and regulates some of the most critical terrestrial environmental services including biogeochemical cycles and delivery of nutrients to primary producers, degradation of pollutants, provision of clean water, regulation of atmospheric trace gases, and pest and pathogen control[3, 4]. Tisdall and Oades' pioneering conceptual model[5] linking microbial activity to soil structure was one of the first to show the importance of interactions between biotic and abiotic phases of soil in building this important structural complexity. Subsequent work has shown that the effect of microbial activity on soil structure is particularly strong at scales that regulate convective and diffusive flow rates, and the balance of air and water at any given matric potential[6]. Not only does microbial activity impact on soil structure, but it does so in a way that creates a feedback on the magnitude and nature of microbial activity.

Such non-linear feedback systems are a necessary condition for the spontaneous emergence of organisation (self-organisation) that is observable at the whole-system level in many complex physical, chemical and biological systems[6]. There is evidence that the soil-microbe complex is self-organising. Accordingly, micro-structural architecture and the resulting critical properties of soil emerge spontaneously from preferential reinforcement against stochastic disturbance of microenvironments that support higher levels of microbial activity (due *e.g.* to higher production

of extracellular polymers). Systems displaying such "organised complexity"[7] are irreducible, presenting particular challenges to identifying causal mechanisms and designing interventions that direct the state of the system. This suggests that the multivariate nature of soil-microbe systems place severe combinatorial constraints on factorial experimental approaches that seek to link OC to soil properties. In such cases, a dynamical systems approach is necessary, where hypotheses are captured in mathematical models, and these hypotheses, and the model structure and parameters, are iterated with experimental data on system evolution. The hypotheses constrain the design of factorial experiments and are in turn constrained by the resulting data.

In this paper, we integrate biological and physical data relating to dynamics of the soil system with mathematical modelling. This approach is used to interpret results from a unique long-term field-experiment in terms of the mechanisms linking OC to emergence of critical soil properties that support NPP and that are implicated in land-climate feedbacks. The experiment is part of the Highfield Ley-Arable Experiment[8] at Rothamsted Research, Harpenden, U.K. and the treatments we use for this study are grassland, arable, and bare fallow (soil kept free of plants and added nutrients since 1959, *i.e.* for 60 years). To study the dynamics of emergence, we also included reversion treatments, in which subplots of degraded bare fallow soil were converted to management under either grassland and arable production. We followed the change in the biophysical properties of the soil over a 10-year period, using the data to infer mechanisms underlying the re-emergence in degraded soil of critical functions.

Results

Soil management is associated with changes in fine-scale connected porosity

- Highfield soils exhibit significantly different structure when considered at the µm-scale. Grassland and arable soils have significantly greater porosity, a wider range of pore sizes and greater pore connectivity compared to bare fallow soil[9]. To assess the influence of soil management upon structure at scales relevant to microbes (10^0-10^2 µm), we generated X-ray Computed Tomography (CT) images at 1.5 µm resolution, requiring imaging of 0.7 – 2.0 mm

diameter soil aggregates. We studied factors associated with connected porosity in detail, since it exerts a strong influence upon diffusive flow in porous materials[11], influencing delivery of nutrients and O_2 to microbial cells. Connected pores within networks can assessed from binary images derived from X-ray CT using Minkowski functions[12], basic geometric measures defined for binary structures. One of these, the Euler number [$\chi(d)$, where d represents the pore diameter] is a well-defined characteristic related to pore space topology and shown to be critical to hydraulic properties[13]. In three dimensions, $\chi(d)$ is defined as the number of isolated pores (of diameter, d) minus the number of redundant connections within the pore space, plus the number of enclosed pores[14]. Using this approach, we estimated Euler number density [$\chi(d)/V$, where V represents the image volume] of the pore network of aggregates from each Highfield soil. The resulting Euler connectivity functions for each soil are shown in Fig. S2. For connected pores $\chi(d)/V < 0$, the value is positive for unconnected pores. $\chi(d)/V = 0$ represents a critical threshold (d_{crit}) describing the maximum pore throat size of connected pores controlling hydraulic conductivity[12]. All structural parameters listed above were highly correlated. We therefore chose porosity and d_{crit} as measures of pore topology since their implications are readily defined and they are expected to be of direct relevance to cells within the soil matrix as they are likely to control advective and diffusional processes within the soils. Mean estimates (± standard error) of d_{crit} were 9.7 ± 0.37 μm for grassland soils, 7.2 ± 0.26 μm for arable soils, and 3.1 ± 0.76 μm for bare fallowed soils. There was a significant effect of soil treatment upon d_{crit} ($F_{2,6} = 42.3$, $p < 0.001$) and all treatment means were significantly different from the others (smallest difference, grassland *versus* arable, $Q = 4.99$, $p = 0.029$). Porosity estimates from X-ray CT (Table 1) were used to derive diffusion coefficients for solutes within saturated soil aggregates, relative to unconstrained solute diffusion in water (D/D_0). For grassland soils, mean D/D_0 was determined at 0.399 ± 0.014, 0.285 ± 0.009 for arable and 0.161 ± 0.001 for bare fallow. These estimates were significantly different ($F_{2,70} = 106.4$, $p < 0.001$). Normalised diffusion coefficients for each treatment were all significantly different from each other ($p < 0.001$ for all comparisons).

Soil is essentially a non-equilibrium metabolic system embedded within a dynamic physical matrix, and its dynamical state can be characterised by three properties: capacity (potential flux), metabolic efficiency, and resilience[10]. Therefore, we present the results of our physical analyses on a phase diagram representing capacity and resilience, using metagenomic data to assess metabolic efficiency. Capacity is quantified by simulating the hydraulic conductivity of each soil when the microscale structure is saturated with water. This measures the connectedness of pore space and the maximum potential flow rate at which resources can move through pore networks. Resilience is measured as the total microscale connected porosity - a measure of the storage capacity of both water and soluble nutrients associated with each soil system. This store can be drawn on when input rates are limiting. Fig. 1 shows the location of the experimental soils on the phase diagram. Our observations associate permanent grassland, established in 1838, with both a high capacity and high resilience. In turn, soil from which all inputs (bare fallowed soil) have been excluded since 1959 has a severely limited capacity to transport nutrients and reduced resilience. Soil managed since 1948 under continuous wheat is located approximately mid-way between the two.

The fraction of anoxic volume in the soil from each treatment was estimated using a multi-phase lattice-Boltzmann approach[15, 16] with gaseous oxygen (O_2) dissolving at water-air interfaces prior to diffusing in liquid water. The same potential respiration rate is assumed for all points on the pore surfaces in CT images, and dependence of respiration on OC and O_2 is used to simulate the anoxic fraction of all reactive sites under different soil moisture. The results (Fig. 2) indicate that the predicted anoxic fraction is significantly lower in grassland soil, compared with arable and bare fallowed soils – the latter is predicted to have the highest fraction of anoxic volume at all moisture contents. Microorganisms in the different soils are therefore likely to experience markedly different hydraulic environments particularly in degraded bare fallow soils where reduced delivery of soluble nutrients and dissolved O_2 is predicted compared to grassland soils, resulting from constraints placed upon diffusive flow by the reduced connected porosity and d_{crit}.

These structural analyses were extended to degraded soil converted in 2007 after 48 years of bare fallow management to grassland and arable, to explore the potential to induce recovery of

biophysical functioning in degraded soil. Testing treatment effects upon connected porosity between 2012 – 2018 inclusive (square-root transformed to stabilize variances) by analysis of covariance, employing time as a covariate, indicated no significant heterogeneity of slopes ($F_{2,75}$= 0.537, p = 0.587). An equal slopes model indicated a significant effect of land management upon connected porosity (ANCOVA, $F_{2,72}$= 26.2, p < 0.001). Holm-Šidák multiple pair-wise comparisons indicated that connected porosity generated in grassland soils ($mean_{adjusted}$, 0.079) was significantly greater than in either unconverted bare fallow ($mean_{adjusted}$, 0.010) or converted arable ($mean_{adjusted}$, 0.025) soils (smallest difference, t = 4.79, p< 0.001). A significant difference between connected porosity generated in arable and bare fallow soils was also apparent (t = 2.30, p = 0.024). No significant differences were detected when the complete 2008 - 2018 data were included, suggesting that significant differences only become apparent after a period of at least five years *post* conversion. Soil converted to grassland responded faster than soil converted to arable, with 33% of the porosity recovered ten years after conversion in the former compared with only 13% in the latter (Fig. 3). The potential role of OC in the observed behaviour was explored by comparing the values of porosity with soil OC content. There was a clear non-linear relationship between OC inputs to soil and connected porosity, with all soils described in this study following the same trend (Fig. 4).

Soil management is associated with shifts in microbiome community structure - Chao-1 Prokaryote OTU richness estimates (S_{Chao1}) for each treatment ranged from 562 – 578 (mean, 570) for grassland, 530 - 547 (mean, 540) for arable, and 482 - 542 (mean, 513) for bare fallow soils. There was a significant effect of soil treatment upon S_{Chao1} (ANOVA, $F_{2,6}$ = 7.6, p = 0.023), the difference between grassland and bare fallow mean richness was significant (Q = 5.49, p = 0.019) but there was no significant difference between arable and grassland or arable and bare fallowed soils. Grassland soils also exhibited the largest Fungal OTU richness, range 35 – 44 (mean, 39) compared to either arable (range, 19 – 27, mean 24) or bare fallowed (range 17

– 27, mean 23) soils. There was again a significant treatment effect upon S_{Chao1} ($F_{2,6}$ = 11.8, p = 0.008) and pair-wise comparison of treatments indicated grassland was significantly more rich in fungal OTUs than either arable or bare fallowed soils (smallest difference, Q = 5.68, p = 0.017), but there was no difference between arable and bare fallowed soils. Weighted UniFrac distance-based comparison of β-diversity (Figure 5) indicated significant effects of soil management upon both prokaryotic (PERMANOVA, *pseudo-*$F_{2,6}$ = 15.5, p_{perm} <0.0001) and fungal (*pseudo-*$F_{2,6}$ = 19.0, p_{perm} = 0.0032) community structures. Prokaryote communities were significantly different between all three treatments (smallest difference, *pseudo-t* = 2.9, p_{MC} < 0.0001) but fungal communities in arable and bare fallowed soils did not differ (*pseudo-t* = 1.7, p_{MC} = 0.111), but both were significantly different from the grassland community (smallest difference, *pseudo-t* = 5.0, p_{MC} = 0.0015). Inspection of individual fungal OTU abundance indicated that this was due to several OTUs, including *Rhizophagus irregularis* and other Glomeromycetes, Agaricomycetidae, Onygenales, Eurotiomycetidae, Aspergillaceae and Atheliaceae, were all abundant in grassland soils but not detected in either arable or bare fallowed soil: arbuscular mycorrhizal *R. irregularis*, for example, had a mean abundance in grassland soils of 3.5 x 10^5, but was not detected in the other soils. This large, qualitative, difference between the soils is consistent with the effect of soil tillage[17, 18] upon fungal communities. Since prokaryotes appeared to be less sensitive to the effects of tillage than fungi, the effects of soil management upon prokaryotic communities were studies in detail.

Prokaryotic Community - Biomarker analysis, using a Random Forest machine learning classification of OTUs identified by taxonomic binning of reads across the three treatments (Fig. 6A), indicated that communities in grassland soils were characterized by Rhizobiaceae including *Bradyrhizobium* spp. and *Rhizobium leguminosarum* as well as the planctomycete *Blastopirellula*. At the other extreme, taxa characteristic of degraded, low input bare fallow soils were *Gemmatimonas*, an organism related to the aromatic compound degrader *Methylibium* and the actinomycete *Sporichthya*. The influence of nitrogenous fertilization was evident from the organisms identified

as characteristic of arable soils: nitrite-oxidizing *Nitrospira* spp. were particularly characteristic of these soils together with the denitrifying *Rhodanobacter*.

16S rRNA-contingent phylogenetic diversity based upon phylogenetic placement of exact sequence variants for each treatment was compared using Kantorovich-Rubinstein (KR) distance metrics. PERMANOVA identified a significant effect of treatment (*pseudo-*$F_{2,6}$ = 17.9, p_{perm}<0.0001) and all *post hoc* comparisons were significantly different (smallest difference: bare fallow *vs*. arable, *pseudo-t* = 3.2, p_{MC} = 0.0018) consistent with the weighted UniFrac approach described above. Principal coordinates analysis (PCoA) was used to present an unconstrained view of differences in 16S rRNA-based microbiome assemblages (Fig. S4) using KR distance. The first two principal coordinates clearly separated treatments and the ordination accounted for 89% of total variation across the first two axes. Distance-based linear modelling (distLM) was used to model the relationship between the 16S rRNA-contingent community structure (using KR distance) and the measured edaphic variables shown in Table 2. All combinations of variables were considered: the most parsimonious model, identified using Bayesian information criterion (BIC), was a combination of the chemical factors pH, %C, %N and extractable P. Distance-based redundancy analysis (dbRDA) indicated that the model accounted for 84% of total variation on the first two axes (Figure 6B). Separation of treatments on the first dbRDA axis (accounting for 84% of fitted and 75% of total variation) was associated most highly with extractable P (r = -0.81; marginal test, *pseudo-F* = 7.4, p_{perm} = 0.013) and %C (r = -0.53; marginal test, *pseudo-F* = 12.2, p_{perm} = 0.0035), both greatest in grassland soils and least in bare fallowed soils. The second axis, accounting for far less variation (10% of fitted and 9% of total) was most highly associated with %C (r = -0.88) and %N (r = 0.41; marginal test, *pseudo-F* = 11.3, p_{perm} = 0.004). Using the four chemical edaphic parameters to model the distribution of treatments, the addition of neither porosity (sequential test, *pseudo-F* = 0.7, p_{perm} = 0.565) nor d_{crit} (sequential test, *pseudo-F* = 0.5, p_{perm} = 0.691) accounted for a significant amount of additional variation.

Soil management is associated with shifts in microbiome functional potential - A total of 1,197 KEGG orthologs were identified as having significantly different abundance between the soils (described in detail in Figs. S6 – S11). We adopted a similar approach to analysing the effects of soil management upon microbiome function, determined by binning reads to KEGG orthologs, as for the effect upon community structure. Multivariate ortholog analysis was based upon Hellinger distance, calculated from square root-transformed ortholog abundance. PERMANOVA identified a significant effect of treatment upon ortholog assemblage (*pseudo-*$F_{2,6}$ = 26.8, p_{perm}<0.0001) and all *post hoc* comparisons were significant (smallest difference: arable – bare fallow, *pseudo-t* = 3.6, p_{MC} = 0.0006). PCoA again clearly separated the treatments, the first two axes accounting for 91% of total variation (Fig. S5). The most parsimonious model identified by distLM included a combination of both chemical and physical edaphic variables; namely pH, %N, porosity and d_{crit}. Using these variables, dbRDA (Figure 7) showed clear separation between the treatments on the primary axis (accounting for 95% of fitted and 83% of total variation). Both edaphic variables most highly associated with this axis were physical parameters, porosity (r = -0.89; marginal test, *pseudo-F* = 24.7, p_{perm} = 0.0009) and d_{crit} (r = -0.38; marginal test, *pseudo-F* = 15.2, p_{perm} = 0.0021). Both variables were greatest in grassland soil and least in bare fallowed soil. The treatments showed little separation on the second axis, which accounted for only 2.8% of fitted and 2.4% of total variation). Both edaphic variables associated most highly with this second axis were chemical, %N (r = -0.86; marginal test, *pseudo-F* = 0.4, p_{perm} = 0.632) and pH (r = 0.41; marginal test, *pseudo-F* = 13.9, p_{perm} = 0.0036). Using these four edaphic parameters to model the distribution of treatments, neither the addition of %C (sequential test, *pseudo-F* = 1.9, p_{perm} = 0.179) nor extractable P (sequential test, *pseudo-F* = 2.2, p_{perm} = 0.121) accounted for a significant amount of additional variation.

Consideration of changes in individual gene abundance across the three treatments indicated clear shifts in both cellular behaviour and metabolic potential, dependent upon treatment (Figure 8). For cell behaviour, genes coding for chemotaxis and twitching motility were more abundant in

arable, and particularly bare fallowed soil compared to grassland soil, as were genes associated with the type II protein secretion system (T2SS), suggesting a greater reliance upon exoenzymes in these soils. Consistent with this latter observation, several genes coding for exoenzymes were more abundant in these soils, including *abnA* (glucosyl hydrolase [GH] family 43 endo-arabinanase), *chiE* (GH family 18 chitinase) and *chiF* and *chiG* (both GH family 19 chitinases) associated with carbohydrate metabolism, and *dmsA* and *dmsB* (dimethyl sulfoxide reductase) associated with sulfur metabolism.

The increase in abundance of *dmsAB* was also part of a general trend of an increase in genes associated with dissimilatory anaerobic metabolism of N and S in arable and bare fallowed soil combined with reductions in genes associated with assimilatory pathways. Nitrification-associated genes were most abundant in arable soils, and genes associated with dissimilatory reduction of nitrate and sulfate most abundant in bare fallowed soils. There was also an increase in genes associated with anaerobic degradation of aromatic compounds in arable and bare fallowed soil. Transport pathways also differed between treatments with genes associated with ATP-binding cassette (ABC) transporter pathways of glycerol and urea being most abundant in grassland soil and least abundant in bare fallowed soil while genes associated with the ABC transport pathway for glutathione and the *N*-acetylglucosamine phosphotransferase pathway exhibited the opposite trend.

Discussion

We have presented new results on the influence of different management practises on soil OC and shown how this affects the capacity, efficiency and resilience of soil systems. These properties relate to the capacity of soil to support NPP, the potential for GHG production and the ability to resist perturbations in water and nutrient inputs. Using a unique and long-term soil restoration experiment, we also present the different extents to which these same management practises can recover critical functions over time in degraded soil. The results can be interpreted in terms of an

existing theory for self-organisation[6] that predicts biophysical functioning emerges from interaction between biological and physical processes by preferential stabilisation of metabolically-favourable microsites in soil. This interpretation predicts that soils which are more metabolically active will generate higher and more connected microscale porosity; confirmed by our analyses.

Systematic changes were observed in community taxonomy and function in response to land management. Taxonomic shifts were consistent with observed Phylum- and Class-level traits in Prokaryotes associated with soil nutrient status (OC, total N *etc.*); functional shifts were also related to nutrient status and, saliently, changes in soil physical structure (pore topology) controlling gaseous and nutrient diffusion. The increase in genes associated with less efficient anaerobic processes in arable and bare fallowed soil can be considered a response to reduced diffusion of O_2 in these progressively more poorly connected pore networks. Other responses, such as the increase in gene abundance for chemotaxis and protein secretion, may also be responses to reduced diffusion of soluble nutrients – and hence a requirement to search out nutrients – or avoidance of anaerobic niches within the soil. Microbial community structure is often considered as a balance of cooperative behaviours between individuals, mediated by "public goods" or soluble nutrients arising from leaky processes (nutrients which are lost through the outer membrane or released by cell lysis) or the activity of exoenzymes[19, 20]. Producers of public goods support populations of "cheaters" which exploit goods without contributing to them. In well-mixed systems, cheaters maintain a competitive advantage over producers, but this advantage is lost in structured environments where diffusive constraints are manifest[21]. In this context, the increase of T2SS and arabinanase and chitinase exoenzyme genes in arable and bare fallowed soils may be a response to reduced delivery of soluble nutrients by advective flow and diffusion to cheaters, and thus an increase in abundance of producer organisms. Additionally, the reduced diffusive processes predicted for arable and particularly bare fallowed soil may result in an increased efficiency of exoenzymes since reduced diffusion allows for a greater accumulation of product near producer organisms[22]. Thus, production of exoenzymes, and cell motility as a searching or avoidance

behaviour provide adaptations in response to spatially constrained circumstances arising from reduced pore connectivity as a result of carbon loss in the arable and bare fallowed soils.

We have highlighted capacity, efficiency and resilience of the soil-microbe system as key properties to focus on because they map directly on to NPP and agricultural yields, GHG emissions, water and OC storage. These critical properties link land-use and climate. The capacity of soil measures how quickly water and nutrients are transported to plant roots and energy to microbes. Efficiency relates to the availability and transformation of such nutrients, and to the production of important greenhouse gases including N_2O and CH_4, which are principally products of anaerobic metabolism. Higher efficiency equates to more nutrients being stored and assimilated (as productivity), and less being lost as GHG. Resilience is related to how much water and soluble nutrients are stored in soil and available for use by the system when input rates become limiting.

The finding that soil under grassland management has significantly higher capacity, efficiency and resilience compared with arable or bare fallowed treatments is correlated with greater OC storage. Furthermore, the rate of recovery of degraded soil is also linked to this OC storage. Our experiments cannot distinguish between OC flux or storage as the dominant mechanism supporting improved soil functioning. However, interpreting results in terms of soil remodelling through self-organizing processes, we predict that the biophysical state of soil and rate of change of that state will both be related to cumulative metabolic activity.

Our data are consistent with recovery rate being limited by cumulative soil metabolism: soil OC content acts as a diagnostic for this. This raises the important question of what limits soil metabolism, and how it can be manipulated in a given context to maximise the rate of soil recovery. We know both anaerobic niches and physical dislocation of microbes from resources result from low pore connectivity, and both significantly limit soil metabolism. We also know soil recovery is linked to a more voluminous and better-connected pore space and significantly lower levels of anaerobic respiration. We speculate that the rate-limiting factor in recovery of degraded soil is the process of microbially-mediated micro-structure remodelling. We hypothesise this would be soil texture-dependent. Sandy-textured soil would be less able to recover compared to soils with

312 higher fractions of silt and clay, where remodelling fine-scale structure is inherently more feasible
313 due to a greater proportion of "raw materials" to enable such fine-scale architecture to be manifest.
314 It is also likely to be dependent on the quality and quantity of organic amendments to soil,
315 especially in relation to the latent energy contained in them. This is apparent in our data, though
316 we are not able to distinguish between the relative importance of each.

317 Tillage is known to contribute to decreases in soil OC, and the most effective recovery rate and
318 highest metabolizing end-state in our data was achieved with management under grassland
319 without tillage. Tillage has the effect of significantly changing the distribution of
320 microenvironments in soil through increased aeration. This results in the immediate release of
321 physical and chemical constraints on C metabolism and therefore to loss of soil OC. More
322 importantly, rearrangement of microenvironments *i.e.* within and between soil macro- and micro-
323 aggregates will have the effect of "re-setting" the microbial remodelling of the soil
324 microarchitecture, slowing down the recovery of connected pore space and longer-term cumulative
325 metabolism.

326 This new interpretation of the role of nutritional and physical management of soil is a step towards
327 a more general theory of soil. Such a theory is needed to help synthesize data and knowledge on
328 the physical, chemical and biological properties of soil that have historically been studied in
329 isolation. Theory leading to quantitative prediction is also essential in seeking synergistic
330 interventions that recognise the interplay between capacity, efficiency and resilience of soil, and to
331 avoid the unintended consequences of land management that are directing us towards systemic
332 collapse of productive land and an amenable climate.

333 Methods
334

335 *Soils* – Identifying the effects of losses of soil organic carbon arising from agricultural practice
336 upon the taxonomic composition and function of soil microbial communities is not trivial since
337 carbon turnover in soil typically occurs over decennial temporal scales: for example, estimated

half-lives of carbon in sandy loam and silty clay loam soils in the United Kingdom are 12 and 20 years respectively[23]. Studies of the effects of persistent soil management must account for such long residence times if they are to assess the maximal change in the community[24]. Clearly, this limits the practicality of laboratory-based experiments in determining the effects of land management upon soil communities but long-term, controlled field manipulations lasting several decades provide opportunities to investigate community responses to changes in soil organic carbon[25]. One such example is the Rothamsted Highfield Ley-Arable experiment (00:21:48 °W, 51:48:18 °N) set on soil that has been under permanent grass since at least 1838. The soil is a silty clay loam (25% clay: 62% silt: 13% sand) (Chromic Luvisol according to FAO criteria). At the time of sampling, arable plots had been under continuous wheat rotation (winter wheat, *Triticum aestivum* L., most recently Hereward seed coated with Redigo® Deter® combination insecticide/fungicide treatment, Bayer CropScience) and receiving ammonium nitrate fertilization to provide approximately 220 kg-N ha^{-1} $annum^{-1}$, and additional 250 kg-K ha^{-1} and 65 kg-P ha^{-1} every three years for 62 years, bare fallow plots had been maintained crop- and weed-free by regular tilling for 52 years, and grassland plots had been maintained as a managed sward of mixed grasses and forbs for over 200 years: all plots are considered now to be in quasi-equilibrium[26]. Physical and biological data has already been reported for these soils (Table I). The experiment compares the original grassland with arable management (established in 1948) as well as bare fallowed soil kept free of vegetation and other organic inputs (established in 1959). Over this period, the bare fallowed soils have become depleted in more labile organic carbon and enriched in persistent organic carbon[27] and soil organic carbon has been reduced to a greater extent than in arable soil. There has also been an observable progressive shift, from grassland to arable and bare fallowed soil, in the distribution of organic carbon between different pools in the three soil managements, particularly a relative decline in discrete organic particles independent of stable soil aggregates, and a corresponding increase in the proportion of organic particles encapsulated in stable aggregates[28]. Confirmation of this apparent shift in soil structure has been provided by high-resolution X-ray Computed Tomography[9].

365 *X-ray Computed Tomography and Image Analysis* – Aggregates (0.7 – 2.0 mm)

366 were selected at random from soil collected from each plot of the Highfield experiment. The
367 aggregates were scanned using a Phoenix Nanotom® system (GE Measurement and Control
368 solution, Wunstorf, Germany) operated at 90 kV, a current of 65 µA and at a voxel resolution of
369 1.51 µm. Initial image analysis was performed using Image-J. Images were threshold-adjusted
370 using the bin bi-level threshold approach of Vogel *et al.*[12] *via* the open source software QuantIm
371 (http://www.quantim.ufz.de/). Porosity and mean pore neck size were estimated directly from
372 the threshold-adjusted binary images and Minkowski functions including Euler number ($\chi(d)$,
373 where d is the pore diameter), pore size distribution, pore connectivity and surface area density
374 were determined according to Vogel *et al.*[12].

375 *Calculation of Diffusion in Soil Pore Networks* - The hierarchical soil structures
376 revealed in X-ray CT images indicate that gaseous O_2 in the atmosphere moves into soil primarily
377 through its inter-aggregate pores and is then dissolved in water prior to moving into the aggregates
378 largely by molecular diffusion. Since gaseous O_2 diffuses up to 1000-fold more quickly than O_2
379 dissolved in water, microbial community activity is thus constrained mainly by O_2 diffusion within
380 aggregates. The ability of aggregates to conduct dissolved O_2 and other soluble substrates depends
381 on the intra-aggregate pore geometry, and we quantified it with effective diffusion coefficients
382 calculated directly by mimicking solute movement through the pore geometry using numerical
383 simulations. The movement of solutes, including O_2 and substrates, within the pore geometry is
384 assumed to be diffusion-dominant. For the images illustrated in Fig. S1, the temporal change in
385 solute concentration inside any pore voxel can be calculated using the finite volume approach, as
386 follows:

$$\frac{c_o^{t+\delta t}-c_o^t}{\delta t}=q_w+q_e+q_s+q_n+q_u+q_d,$$

$$q_w=\begin{cases}D\left(c_w^{t+\delta t}-c_o^{t+\delta t}\right) & if\ voxel\ w\ is\ pore\\ 0, & if\ voxel\ w\ is\ solid\end{cases},\ q_e=\begin{cases}D\left(c_e^{t+\delta t}-c_o^{t+\delta t}\right) & if\ voxel\ e\ is\ pore\\ 0, & if\ voxel\ e\ is\ solid\end{cases}$$

$$q_s=\begin{cases}D\left(c_n^{t+\delta t}-c_o^{t+\delta t}\right) & if\ voxel\ s\ is\ pore\\ 0, & if\ voxel\ s\ is\ solid\end{cases},\ q_n=\begin{cases}D\left(c_s^{t+\delta t}-c_o^{t+\delta t}\right) & if\ voxel\ n\ is\ pore\\ 0, & if\ voxel\ n\ is\ solid\end{cases}$$

$$q_d=\begin{cases}D\left(c_d^{t+\delta t}-c_o^{t+\delta t}\right) & if\ voxel\ d\ is\ pore\\ 0, & if\ voxel\ d\ is\ solid\end{cases},\ q_u=\begin{cases}D\left(c_u^{t+\delta t}-c_o^{t+\delta t}\right) & if\ voxel\ u\ is\ pore\\ 0, & if\ voxel\ u\ is\ solid.\end{cases} \quad (1)$$

where c is concentration, q is diffusive flux, D is molecular diffusion of the solute in liquid water, superscripts t and $t+\delta t$ represent time, δt is a time increment, subscript o represents the pore voxel being calculated, and subscripts w, e, s, n, u and d represents the face-to-face neighbours of voxel o on the west, east, south, north, top and bottom sides respectively. Applying Eq. (1) to all pore voxels leads to linear systems which was solved by the bi-conjugate gradient stabilized method[29].

Calculation of Diffusion Coefficients – To calculate the effective diffusion coefficient of each aggregate, we applied a constant concentration C_1 on the top and a constant concentration C_o on the bottom of the image, and then simulated solute diffusion to steady state. The diffusive flux in the three directions in each pore voxel was calculated by Eq. 1. Taking the vertical direction as the z direction for the image, the effective diffusion coefficient of the image was calculated as follows:

$$D_{eff}=\frac{L_z\sum_{i=1}^{N}q_z(x_i)}{N\left(C_1-C_0\right)} \quad (2)$$

where D_{eff} is the effective diffusion coefficient, N is the total number of pore voxels in the simulated images, $q_z(x_i)$ is the vertical diffusive flux in pore voxel centred at location x_i, L_z is the height of the image as shown in Fig. S1. To address the impact of change in pore geometry due to management on the ability of the aggregate to diffuse solute, in result analysis we normalized the effective diffusion coefficient D_{eff} of all solutes by their associated molecular diffusion coefficient in non-constrained water, D.

406 *Modelling of Oxygen Diffusion and Anoxia* - The impact of soil structure on O_2

407 diffusion and its subsequent consumption by microbes under various saturations was studied using

408 pore-scale simulations. We first calculated the spatial distribution and connectedness of different

409 pores and then determined water distributions in pores under different matric potentials (ψ_m). We

410 assumed the soil was initially saturated and then applied a negative pressure p at the bottom to

411 drain water. We assumed the soil was essentially hydrophilic in that only pores whose associated

412 capillary pressure p_c, calculated by $p_c = \sigma / r$ with σ being water-air surface tension, is less than p

413 and that they form clusters which stretch from the top to the bottom of the structure can be drained.

414 Fig. 3A shows an example illustrating water distribution in the structure calculated using the

415 method described above when the saturation is 55%.

416 Once the water distribution was determined for a given ψ_m, we treated the water-air interfaces

417 inside the structure as a boundary at which gaseous O_2 dissolves and then moves toward the solid-

418 water interface to be reduced by microbial reactions. The partial pressure of gaseous O_2 in the

419 simulated structure was assumed to be constant. Movement of dissolved O_2 in the liquid water was

420 simulated using the following diffusion-reaction equation:

421
$$\frac{\partial c}{\partial t} = \nabla D \nabla c - s, \qquad c\big|_{\Gamma_{aw}} = c_s \qquad (1)$$

422 where c is concentration of the dissolved O_2, D is molecular diffusion coefficient of O_2 in water,

423 Γ_{aw} is the air-water interface, s is microbial consumption, c_s is the saturated dissolved O_2

424 concentration at the water-air interface calculated from Henry's law, $c_s = p_o / H$ in which H is the

425 Henry constant and p_o is the partial pressure of the gaseous O_2 inside the structure. Microbial

426 consumption was assumed to occur in water-filled voxels adjacent to the water-solid wall and

427 described by the following Monod kinetic equation:

$$s = m_c k_0 \frac{[C]}{k_C + [C]} \frac{c}{k_O + c}, \quad (2)$$

where m_c is microbial biomass, k_0 is kinetic parameter, $[C]$ is the concentration of dissolved carbon. Since we are interested in impact of soil structure on development of anaerobic sites, we simulated O_2 diffusion and reduction to steady state. In all simulations, we normalized Eqs. (1) and (2) as follows

$$\frac{\partial c'}{\partial t'} = \nabla D' \nabla c' - s',$$
$$c'|_{\Gamma_{aw}} = 1,$$
$$s' = k' \frac{c}{k_o' + c}$$

where $t' = t/T_0$, $D' = DT_0/L^2$, $c' = c/c_s$ and $k' = m_c k_0 T_0 [C]/(k_c + [C])$ in which L is the side length of the voxels and T_0 is a characteristic chosen to make $D' = 1$ in our simulations.

The above equation was solved by a finite volume method with each water-filled voxel being the element used to calculate the mass balance. In all simulations, water was assumed be initially free of O_2 and we simulated the system to steady state. As the development of anaerobic areas was a balance between the ability of soil to diffuse dissolved O_2 and the microbial consumption rate, to elucidate that the relative anaerobicity of soils under the same ψ_m is the consequence of their structures and does not change with microbial reactive rate, we simulated two scenarios: a fast microbial decomposition (k'= 1x10^{-2}) and a slow microbial decomposition (k'= 1x10^{-4}). For each scenario, once the system was deemed to have reached a steady state, we sampled sites where concentration of dimension-less dissolved O_2 was less than 20% assuming them be at anaerobic condition[30]. Fig. 3B shows an illustrative example of the location of anaerobic areas simulated by the above method in which soil particles were made transparent. We repeated the procedure to achieve different water distributions calculated by varying ψ_m and then calculated the proportional change in the volumetric anaerobic sites with the ψ_m for both the fast and slow microbial reactions. The results are shown in Figure 2 for soil samples taken from all treatments.

Modelling of organic carbon dynamics in soil - We used RothC-26.3[31] to model the turnover of soil organic carbon in the experimental soils, accounting for the effects of soil type, plant cover and historical temperature and moisture content on organic carbon turnover processes. We used the same inputs of organic carbon to the soil that were used in Johnston *et al.*[23]. To obtain the starting soil carbon of 63.6 Mg-C ha^{-1}, a carbon input to the soil from plant debris, roots, and root exudates was 2.7 Mg-C ha^{-1}, with the inert organic matter being 3.0 Mg-C ha^{-1}. The incoming carbon from plant residues were assumed to have decomposable plant material and resistant plant material in the proportion 0.59 and 0.41, respectively, these are the default proportions for arable cropping and managed grassland. For the first 12 years after the experiment started, the grass was grazed by sheep before the treatment changed to a grass/clover sward harvested three or four times per year for conservation. For this reason, the grass treatments received carbon inputs of 5 Mg-C ha^{-1} $annum^{-1}$ between 1949 and 1960, or 4 Mg-C ha^{-1} $annum^{-1}$ between 1961 and 2016. The arable treatments received a carbon input of 1.4 Mg-C ha^{-1} $annum^{-1}$ and the bare fallow treatments received no inputs of carbon to the soil.

DNA Extraction and Metagenome Sequencing - Soil was collected from triplicate plots for each treatment to a depth of 10 cm using a 3-cm diameter corer. The top 2 cm of soil containing root mats and other plant detritus was discarded. Ten cores per plot were pooled and thoroughly mixed whilst sieving through a 2-mm mesh; samples were then frozen at -80 °C. All implements were cleaned with 70% ethanol between sampling/sieving soil from each plot. Soil community DNA was extracted from a minimum of 2 g soil using the MoBio PowerSoil® DNA isolation kit (Mo Bio Laboratories, Inc. Carlsbad, CA) with three replicates for each soil treatment. When necessary, extracts from individual replicates were pooled to provide sufficient material for sequencing. 10 µg of high-quality DNA was provided for sequencing for each of the nine plots. Shotgun metagenomic sequencing of DNA was provided by Illumina® (Cambridge, UK) using a HiSeq™ 2000 sequencing platform, generating 150-base, paired-end reads. The generated sequences were limited to a minimum quality score of 25 and a minimum read length of 70-bases

476 using Trimmomatic[32]. After filtering to remove substandard sequences, the average metagenome
477 size for each soil was 4.96x10^8 reads for grassland, 2.86x10^8 for arable and 2.88x10^8 for bare fallow
478 soils. Since differences in library sizes were less than 10-fold, we did not employ rarefaction before
479 comparing the datasets[33]. Details of dataset comparison and bioinformatical analysis are presented
480 in Figs. S6 - S11.

481 *Bioinformatical Analysis of Metagenome Sequences* - To assess general abundance
482 of taxa and genes in metagenomes, we mapped individual metagenomic sequences to the RefSeq
483 non-redundant (NR) protein database held at NCBI (downloaded August 22nd, 2018) using
484 DIAMOND ver. 0.8.27[34] in BLASTX mode using a bitscore cut-off of 55. For each sequence, only
485 the match with the highest bitscore was considered. Sequences not matching the NR database were
486 considered currently unclassified. MEGAN Ultimate ver. 6.10.2[35] was used to associate
487 metagenome sequences with both taxa and Kyoto Encyclopaedia of Genes and Genomes[36]
488 (KEGG) functional orthologs and modules. For taxa, MEGAN was used to establish Prokaryotic
489 and Fungal community assemblages and calculate weighted UniFrac distances[37] between the
490 assemblages associated with each soil treatment. In addition, bacterial communities were also
491 compared based upon the abundance and phylogenetic relatedness of metagenome reads
492 homologous to the 16S rRNA gene. A 16S rRNA profile hidden Markov model (pHMM) was
493 generated based upon an alignment of the set of 4,528 reference sequences associated with
494 paprica[28], built December 2017. Metagenome reads with homology to the 16S rRNA pHMM were
495 identified using hmmsearch[39] with a 1x10^{-5} Expect-value (*E*) cut-off and assigned to branches of
496 fixed maximum likelihood 16S rRNA phylogenetic tree using a phylogenetic placement algorithm,
497 pplacer ver. 1.1alpha10[40]. To assess 16S rRNA gene-based β-diversity in the different soils,
498 Kantorovich-Rubinstein[41] (KR) phylogenetic distance metrics were calculated from phylogenetic
499 placements of metagenome reads using the guppy kr binary (part of the pplacer suite), treating
500 each query as a point mass concentrated on the highest-weight placement. The advantage of the
501 KR distance metric is that it compares gene assemblage distributions on a phylogenetic tree (of

16S rRNA or other genes), in units of nucleotide substitutions *per* site, and is therefore a biologically meaningful approach to comparing communities.

From all of the reads binned to a KEGG orthologous group, we selected those associated with carbohydrate metabolism (ko09101) (including glycolysis/gluconeogenesis (ko00010), citrate cycle (ko00020), pentose phosphate pathway (ko00030), pentose and glucuronate interconversions (ko00040), fructose and mannose metabolism (ko00051), galactose metabolism (ko00052), ascorbate and aldarate metabolism (ko00053), starch and sucrose metabolism (ko00500), amino sugar and nucleotide sugar metabolism (ko00520), pyruvate metabolism (ko00620), glyoxylate and dicarboxylate metabolism (ko00630), propanoate metabolism (ko00640), butanoate metabolism (ko00650), C5-branched dibasic acid metabolism (ko00660), inositol phosphate metabolism (ko00562)), methane metabolism (ko00680), carbon fixation pathways in prokaryotes (ko00720), nitrogen metabolism (ko00910), sulfur metabolism (ko00920), xenobiotics biodegradation and metabolism (ko09111) (including benzoate degradation (ko00362), aminobenzoate degradation (ko00627), fluorobenzoate degradation (ko00364), chloroalkane and chloroalkene degradation (ko00625), chlorocyclohexane and chlorobenzene degradation (ko00361), toluene degradation (ko00623), xylene degradation (ko00622), nitrotoluene degradation (ko00633), ethylbenzene degradation (ko00642), styrene degradation (ko00643), atrazine degradation (ko00791), caprolactam degradation (ko00930), dioxin degradation (ko00621), naphthalene degradation (ko00626), polycyclic aromatic hydrocarbon degradation (ko00624), furfural degradation (ko00365), steroid degradation (ko00984), metabolism of xenobiotics by cytochrome P450 (ko00980) and drug metabolism – other enzymes (ko00983)), enzyme families (ko09112), membrane transport (ko09131) (including transporters (ko02000), ABC transporters (ko02010), phosphotransferase systems (ko02060), bacterial secretion systems (ko03070) and secretion systems (ko02044)), two-component systems (ko02020 and 02022), biofilm formation – *Vibrio cholerae* (ko05111), - *Pseudomonas aeruginosa* (ko02025), - *Escherichia coli* (ko02026), bacterial chemotaxis (ko02030), bacterial motility proteins (ko02035), and flagellar assembly (ko02040) for detailed study of abundance differences between the soils. Where necessary, KEGG orthologs

were associated with higher-order functions by mapping to the KEGG BRITE functional hierarchy classification. In total, 8,857 KEGG functional orthologs were identified. To identify genes for which a significant difference in abundance between the treatments was observed we used DESeq2[42] which employs a negative binomial generalized linear model to generate maximum-likelihood estimates for each gene's $\log_2$-fold change between conditions. Bayesian shrinkage, based upon a zero-centred normal distribution as a prior, shrinks the $\log_2$-fold change towards zero for genes with low mean counts or a high dispersion in their count distribution. The resulting shrunken fold-changes are used in tests of significance using Wald's method. DESeq2 has been shown to be particularly sensitive to differences in gene abundance on small datasets[33] such as those in this study. Before analysis, 3,930 low abundance features were removed (minimum mean count of 20) as well as 986 features with a low coefficient of variation. Differential abundance of the remaining 3,940 genes was tested for significance employing α=0.05 and a Benjamini-Hochberg false discovery rate (q) of 0.1 to control type I error rate in the face of multiple comparisons. To identify the most diagnostic microorganisms characterising communities of each soil, we used supervised Random Forests[43] (RF), a classification algorithm approach based upon a collection of unpruned decision trees, each built using a bootstrap sample of training data using a randomly selected subset of OTUs. The RF classifier was built by growing 5,000 trees. The prediction performance and confusion matrices were determined using out-of-bag cross-validation (OOBCV). The percent mean decrease in accuracy of the importance matrix was used to select taxa that were most predictive of each microbiome assemblage. DESeq2 and RF were employed as implemented in MicrobiomeAnalyst[44].

Statistical Analysis - One-factor analysis of variance (ANOVA) was employed to test the effect of soil treatment upon d_{crit} and modelled diffusion coefficients arising from X-ray CT, and phylogenetic diversity estimates of α-diversity arising from metagenomic analysis. Where a significant treatment effect was observed, *post hoc* pairwise comparisons were performed using either Tukey's HSD test (Q) employing the Copenhaver & Holland multiple comparisons

555 procedure. These tests were performed in PAST ver. 3.25[45]. One-factor analysis of covariance
556 (ANCOVA) was used to test for treatment effects upon the formation of connected porosity in
557 degraded soil following conversion to either arable or grassland, using time *post* conversion as the
558 covariate. The assumption of homogeneity of slopes was first tested before ANCOVA was used
559 to test for treatment effects using an equal slopes model. *Post hoc* Holm-Šidák multiple pair-wise
560 comparisons were used to establish whether differences in adjusted mean connected porosity
561 between treatments were significant. ANCOVA was performed in SigmaPlot for Windows ver.
562 14.0 (Systat Software Inc., San Jose, CA).

563 For metagenome-associated multivariate data, we initially compared prokaryotic and fungal
564 communities by calculating unrooted phylogenetic Neighbour-nets[46] using weighted UniFrac
565 distances and compared the 16S rRNA-contingent bacterial assemblages using KR distances. KR
566 distance-based analyses were performed after testing for heteroscedasticity using PERMDISP[47].
567 Hypothesis testing was based upon permutational multivariate analysis of variance[48]
568 (PERMANOVA) and *post hoc* pair-wise tests. Differences between treatment were visualized using
569 Principal Coordinates Analysis (PCoA) using the chosen distance measure. To identify
570 associations between chemical and physical edaphic factors and any treatment effects, distance-
571 based linear modelling[49] was used to identify the best combination of edaphic factors to model the
572 multivariate data and the resulting model was visualized using distance-based redundancy
573 analysis. All multivariate tests were performed in PRIMER PERMANOVA+ ver 7.0.13 and
574 probabilities were based upon 99,999 permutations (denoted p_{perm}). For PERMANOVA *post hoc*
575 pair-wise comparisons, since the number of observations was insufficient to allow a reasonable
576 number of permutations, Monte Carlo probabilities (denoted p_{MC}) were calculated based upon an
577 asymptotic permutation distribution[50].

1. IPCC (2019), Climate Change and Land. IPCC Special Report on Climate Change, Desertification, Land Degradation, Sustainable Land Management, Food Security, and Greenhouse gas fluxes in Terrestrial Ecosystems. (2019).
2. Wilpiszeski R. L. *et al.*, Soil aggregate microbial communities: towards understanding microbiome interactions at biologically relevant scales. *Appl. Environ. Microbiol.* **85**, e00324-19. (2019).
3. Haygarth P.M. & Ritz K. The future of soils and land use in the UK: Soil systems for the provision of land-based ecosystem services. *Land Use Policy* **26**, S187-S197 (2009).
4. Lehman R. M. *et al*. Understanding and enhancing soil biological health: the solution for reversing soil degradation. *Sustainability* **7**, 988-1027 (2015).
5. Tisdall J. M. & Oades J. M. Organic matter and water-stable aggregates in soils. *Eur. J. Soil Sci*. **33**, 141-163 (1982).
6. Crawford J. W. *et al*. Microbial diversity affects self-organization of the soil- microbe system with consequences for function. *J. Roy. Soc. Interface* **9**, 1302-1310 (2012).
7. Weaver W. Science and Complexity. *Am. Scientist* **36**, 536-544 (1948).
8. Gregory A. S. *et al*. Long-term management changes topsoil and subsoil organic carbon and nitrogen dynamics in a temperate agricultural system. *Eur. J. Soil Sci*. **67**, 421–430 (2016).
9. Bacq-Labreuil A. *et al*. Effects of cropping systems upon the three-dimensional architecture of soil systems are highly contingent upon texture. *Geoderma* **332**, 73-83 (2018).
10. Liu J., Crawford J. W., Viola R. & Goodman B. A. Prospects for advancing the understanding of complex biochemical systems. *Plant Mol. Biol*. **33**, 573-581 (1997).
11. Köhne J. M., Schlüter S. & Vogel H.-J. Predicting solute transport in structured soil using pore network models. *Vadose Zone J*. **10**, 1082-1096 (2011).
12. Vogel H.-J., Weller U. & Schlüter S. Quantification of soil structure based upon Minkowski functions. *Comput. Geosci*. **36**, 1236-1245 (2010).
13. Vogel H.-J. A numerical experiment on pore size, pore connectivity, water retention, permeability, and solute transport using network models. *Eur. J. Soil Sci*. **51**, 99–105 (2000).
14. Vogel H.-J. Topological characterization of porous media. Pp., 75-92 in *Morphology of Condensed Matter: physics and geometry of spatially complex systems* edited by Mecke K. & Stoyan D. Springer-Verlag, Berlin (2002).
15. Zhang X. & Ren L. Lattice Boltzmann model for agrochemical transport in soils. *J. Contam. Hydrol*. **67**, 27-42 (2003).
16. Zhang X., Deeks L. K., Bengough A. G., Crawford J. W. & Young I. M. Determination of soil hydraulic conductivity with lattice Boltzmann method and soil thin-section technique. *J. Hydrol*. **306**, 59-70 (2005).
17. Brito, I., Goss M. J., de Carvalho M., Chatagnier O. & van Tuinen D. Impact of tillage system on arbuscular mycorrhiza fungal communities in the soil under Mediterranean conditions. *Soil Tillage Res.* **121**, 63-67. (2012).
18. Lu X., Lu X. & Liao Y. Effect of tillage treatment on the diversity of soil arbuscular mycorrhizal fungal and soil aggregate-associated carbon content. *Front. Microbiol.* **9**, article 2986 (2018).
19. Allison S. D. Cheaters, diffusion and nutrients constrain decomposition by microbial enzymes in spatially structured environments. *Ecol. Lett*. **8**, 626-635 (2005).
20. Harrington K. I. & Sanchez A. Eco-evolutionary dynamics of complex social strategies in microbial communities. *Communic. Integrat. Biol*. **7**, e28230 (2014).

21. Allison S. D., Lu L., Kent A. G. & Martiny A. C. Extracellular enzyme production and cheating in *Pseudomonas fluorescens* depend upon diffusion rates. *Front. Microbiol*. **5**, 169 (2014).
22. Allison S. D., Weintraub M. N., Gartner T. B. & Waldrop M. P. Evolutionary-economic principles as regulators of soil enzyme production and ecosystem production. *Soil Enzymol*. **22**, 229-243 (2011).
23. Johnston A. E., Poulton P. R. & Coleman K. Soil organic matter: its importance in sustainable agriculture and carbon dioxide fluxes. *Adv. Agron*. **101**, 1-57 (2009).
24. Shade A *et al*. Fundamentals of microbial community resistance and resilience. *Front. Microbiol*. **3**, article 417 (2012).
25. Schmidt M. W. I. *et al*. Persistence of soil organic matter as an ecosystem property. *Nature* **478**, 49-56 (2011).
26. Wu Y., Kemmitt S., White R. P., Xu J. & Brookes P. C. Carbon dynamics in a 60 year fallowed loamy-sand soil compared to that in a 60 year permanent arable or permanent grassland UK soil. *Plant Soil* **352**, 51-53 (2012).
27. Barré P. *et al*. Quantifying and isolating stable soil organic carbon using long-term bare fallow experiments. *Biogeosciences* **7**, 3839-3850 (2010).
28. Hirsch P. R. *et al*. Starving the soil of plant inputs for 50 years reduces abundance but not diversity of soil bacterial communities. *Soil Biol. Biochem*. **41**, 2021-2024 (2009).
29. van der Vorst H. A. BI-CGSTAB – a fast and smoothly converging variant of BI-CG for the solution of nonsymmetric linear systems. *Siam J. Sci. Statist. Comp*. **13**, 631-644. (1992).
30. Harrison D. E. F. & Pirt S. J. The influence of dissolved oxygen concentration on the respiration and glucose metabolism of *Klebsiella aerogenes* during growth. *J. Gen. Microbiol*. **46**, 193-211 (1967).
31. Coleman K. *et al*. Simulating trends in soil organic carbon in long-term experiments using RothC-26.3. *Geoderma* **81**, 29-44 (1997).
32. Bolger A. M., Lohse M. & Usadel B. Trimmomatic: a flexible trimmer for Illumina sequence data. *Bioinformatics* **30**, 2114-2120 (2014).
33. Weiss S. *et al*. Normalization and microbial differential abundance strategies depend upon data characteristics. *Microbiome* **5**, 27 (2017).
34. Buchfink B., Xie C. & Huson D. H. Fast and sensitive protein alignment using DIAMOND. *Nature Meth*. **12**, 59-60. (2015).
35. Huson D. H. *et al*. MEGAN Community Edition – interactive exploration and analysis of large-scale microbiome sequencing data. *PLoS Comput. Biol*. **12**(6), e1004957 (2016).
36. Kanehisa M., Sato Y., Kawashima M., Furumichi M., Tanabe M. KEGG as a reference resource for gene and protein annotation. *Nucl. Acids Res*. **44**, D457-D462 (2015).
37. Lozupone C., Lladser M. E., Knights D., Stombaugh J. & Knight R. UniFrac: an effective distance metric for microbial community comparison. *ISME J.* **5**, 169-172. (2011).
38. Bowman J.S. & Ducklow H.W. Microbial communities can be described by metabolic structure: a general framework and application to a seasonally variable, depth-stratified microbial community from the Coastal West Antarctic Peninsula. *PLoS ONE* 10.8: e0135868. (2015).
39. Eddy S. R. A new generation of homology search tools based on probabilistic inference. *Genome Inform*. **23**, 205-211. (2009).
40. Matsen F. A., Kodner R. B. & Armbrust E. V. pplacer: linear time maximum-likelihood and Bayesian phylogenetic placement of sequences onto a fixed reference tree. *BMC Bioinformatics* **11**, 538. (2010).

41. Evans S. N. & Matsen F. A. The phylogenetic Kantorovich-Rubinstein metric for environmental sequence samples. *J. Roy. Stat. Soc. Series B Stat. Methodol*. **74**, 569-592. (2012).
42. Love M. I., Huber W. & Anders S. Moderated estimation of fold change and dispersion for RNA-seq data with DESeq2. *Genome Biol*. **15**, 550 (2014).
43. Cutler D. R. *et al*. Random Forests for classification in ecology. *Ecology* **88**, 2783-2792. (2007).
44. Dhariwal A. *et al*. MicrobiomeAnalyst: a web-based tool for comprehensive statistical, visual and meta-analysis of microbiome data. *Nucl. Acids Res*. **45**, W180-W188. (2017).
45. Hammer Ø., Harper D. A. T. & Ryan P. D. PAST: paleontological statistics software package for education and data analysis. *Palaeontologia Electronica* **4**, 9 (2001).
46. Mitra S., Gilbert J. A., Field D. & Huson D. H. Comparison of multiple metagenomes using phylo-genetic networks based on ecological indices. *ISME J*. **4**, 1236-1242 (2010).
47. Anderson M. J. Distance-based tests for homogeneity of multivariate dispersions. *Biometrics* **62**, 245-253 (2006).
48. McArdle B. H. & Anderson M. J. Fitting multivariate models to community data: a comment on distance-based redundancy analysis. *Ecology* **82**, 290-297 (2001).
49. Legendre P. & Anderson M. J. Distance-based redundancy analysis: testing multispecies responses in multifactorial ecological experiments. *Ecol. Monographs* **69**, 1-24 (1999).
50. Anderson M. J. & Robinson J. Generalized discriminant analysis based on distances. *Austr. New Zeal. J. Statis.* **45**, 301-318. (2003).

Acknowledgments: The authors are grateful to David Hughes, Department of Computational and Analytical Sciences at Rothamsted for data and software code curation associated with metagenomic analyses; **Funding:** This research was supported by the United Kingdom's Biotechnology and Biological Science Research Council (BBSRC)-funded Soil to Nutrition strategic program (BBS/E/C/000I0310) and jointly by the Natural Environment Research Council and BBSRC as part of the Achieving Sustainable Agricultural Systems research program (NE/N018125/1 LTS-M). Access to the Highfield Ley-Arable experiment is supported by the UK's Long-Term Experiment National Capability funded by BBSRC (BBS/E/C/000J0300);
Author contributions: All authors played a part in conceptualizing the study and methodology development; AB-L generated and analyzed the X-ray computed tomography of soil pore space under supervision of KR and SJM; ALN performed analyses of metagenomic data and prepared the original draft manuscript and was responsible for data presentation; XZ was responsible for programming and software development associated with modeling of hydraulic conductivity and soil anoxic volume, implementation of computer code and supporting algorithms; KC was responsible for implementation of the RothC-26.3 computer code and supporting algorithms associated with modeling organic carbon in the soils; all authors participated in the development of the final version of the manuscript; **Competing interests:** the authors declare no competing interests; **Data and materials availability:** All data, code, and materials used in this research is available together with extensive chemical, climate and treatment data and history on the *e*-RA database, maintained by Rothamsted Research.

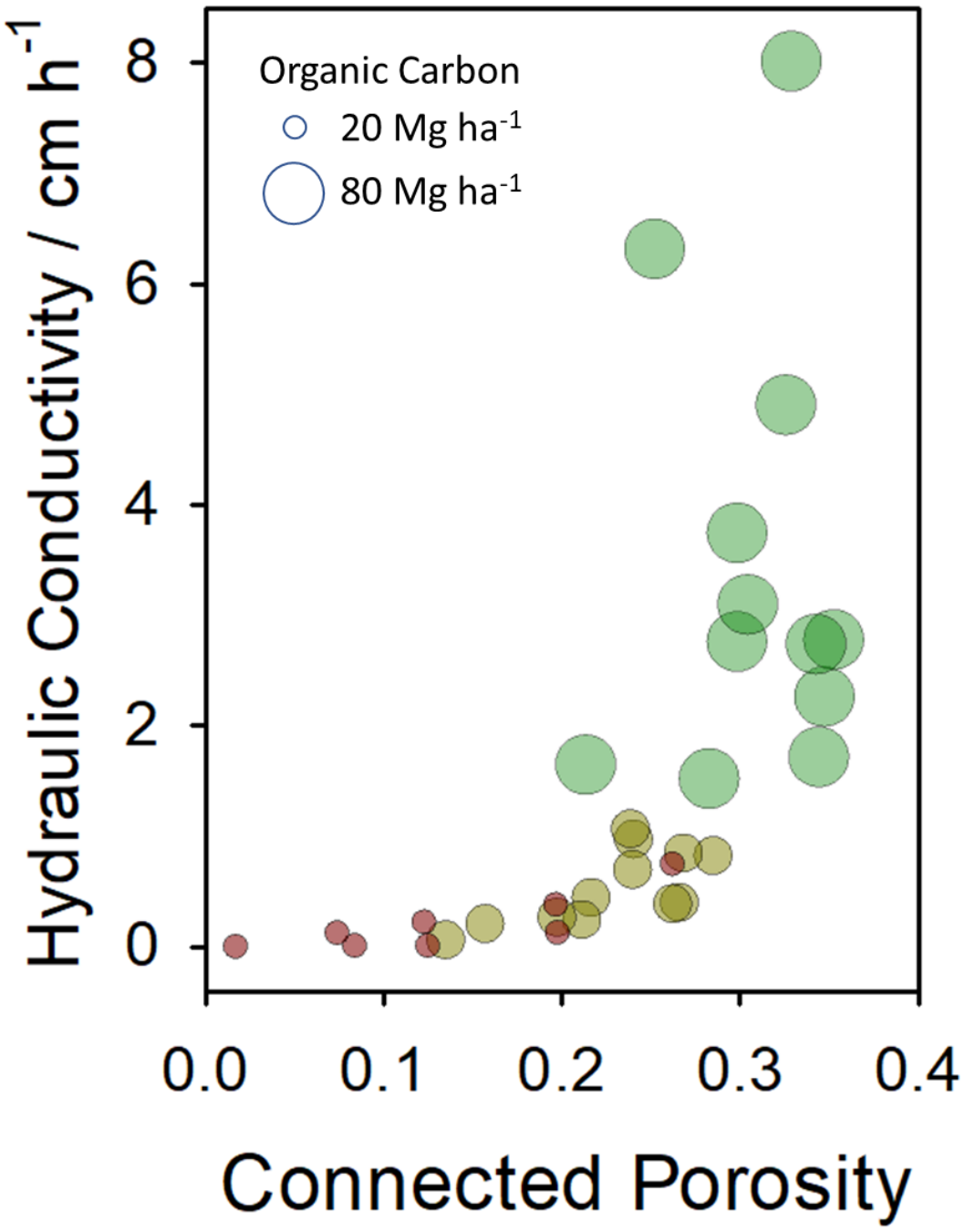

Figure 1. Phase diagram representation of soil resilience and capacity. Soils are described by a combination of the connectivity of pore space, established from X-ray CT (connected porosity) – a measure of system *resilience* relating to storage of water and nutrients, and modelled hydraulic conductivity - a measure of *capacity*, representing the maximum potential movement of resources through pore networks to organisms. Grassland soils (green data points) are characterized as having high pore connectivity and hydraulic conductivity and are associated with the greatest stocks of organic carbon. In contrast, degraded soils (brown data points) are associated with extremely limited connected porosity and hydraulic conductivity and the lowest stocks of organic carbon. Arable soil (dark yellow) is intermediate between these two extremes.

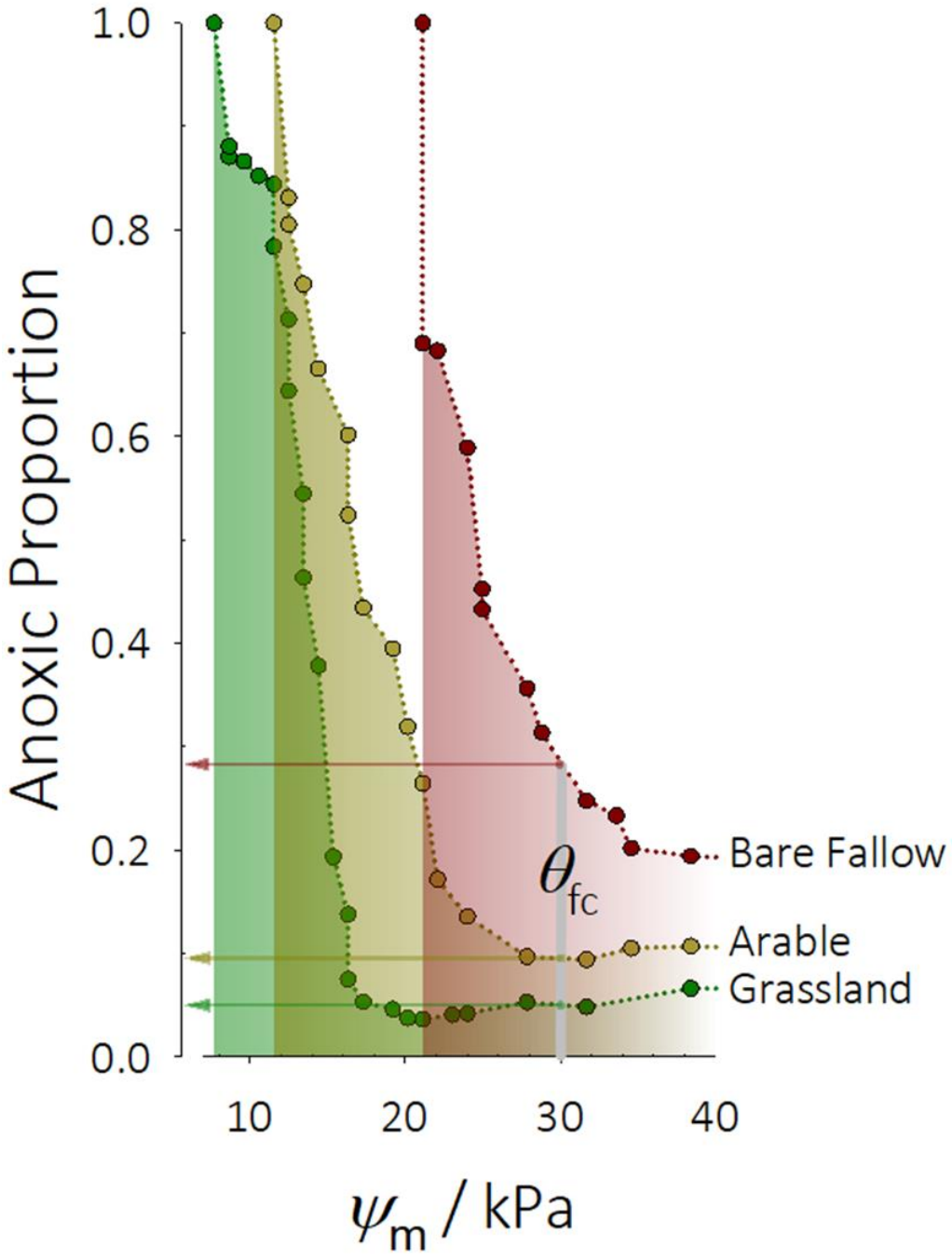

722

723 **Figure 2. Low-carbon, low-connected porosity soil contains much larger volumes of anoxic**
724 **microsites than high-carbon, high-connected porosity soil.** Across a range of matric potential
725 (ψ_m), the predicted volume of anoxic sites is consistently larger in degraded bare fallowed soil
726 (brown data points and shaded region) than arable or grassland (dark yellow and green data points
727 and shaded regions respectively). At field capacity (θ_{fc}), approximately 30% of degraded soil is
728 anoxic, falling to 5% in grassland soil. At 21 kPa degraded soil is completely anoxic while the
729 volume remains between 4-5% in grassland soil. In arable soil 10% of the soil volume is predicted
730 to be anoxic at θ_{fc} – double that in grassland.

731

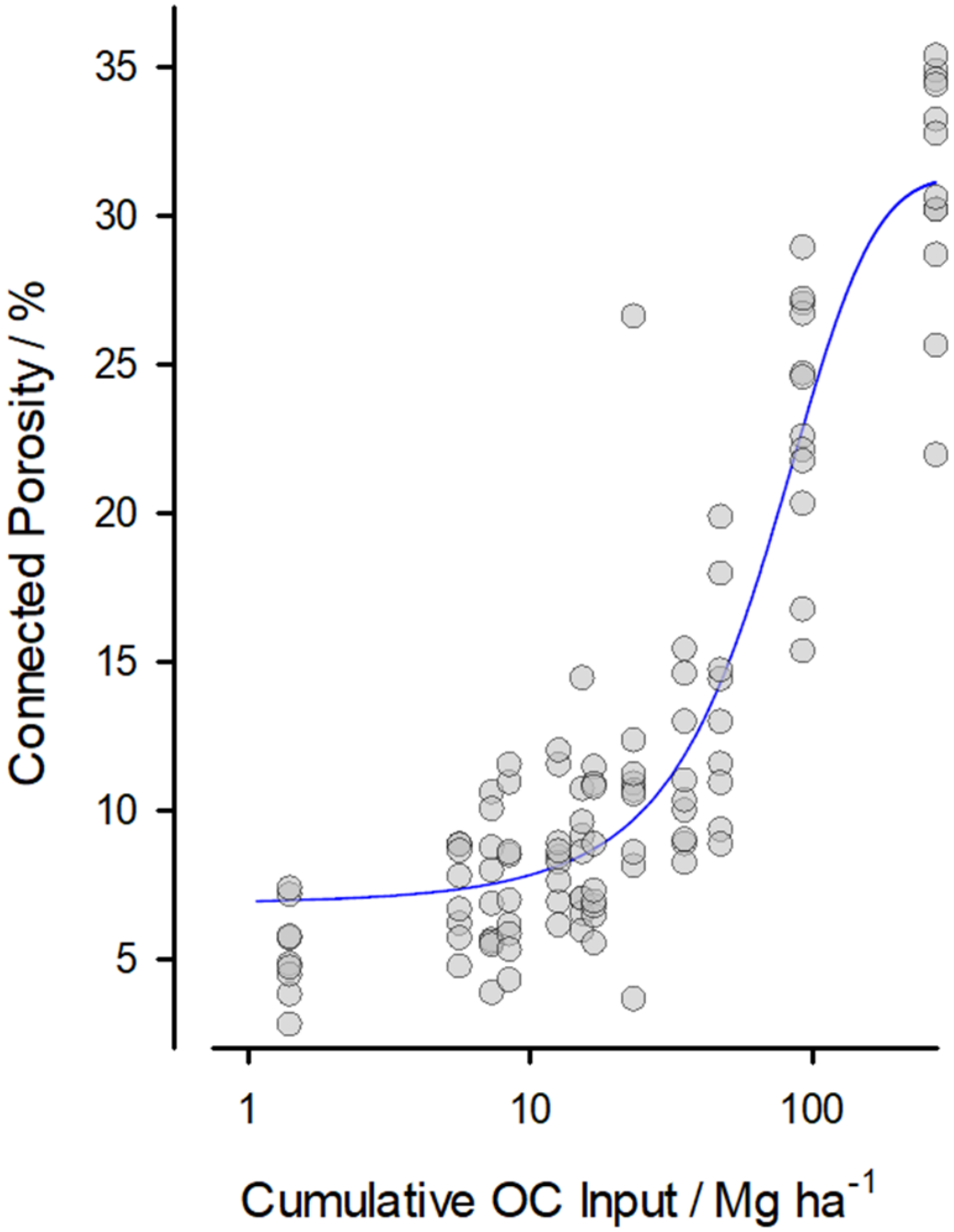

732

733 **Figure 3. Strong association between organic carbon inputs to soil and connected porosity.** The
734 connected pore space in degraded soils converted after 48 years of bare fallow management to
735 either arable or grassland increases in association with the cumulative input of organic carbon
736 (OC) over a decade. Soils managed continuously as either arable (67 years) or grassland (>170
737 years) which have each accumulated over 100 Mg ha^{-1} of organic carbon over their history follow
738 this trend. $R^2 = 0.85$.
739

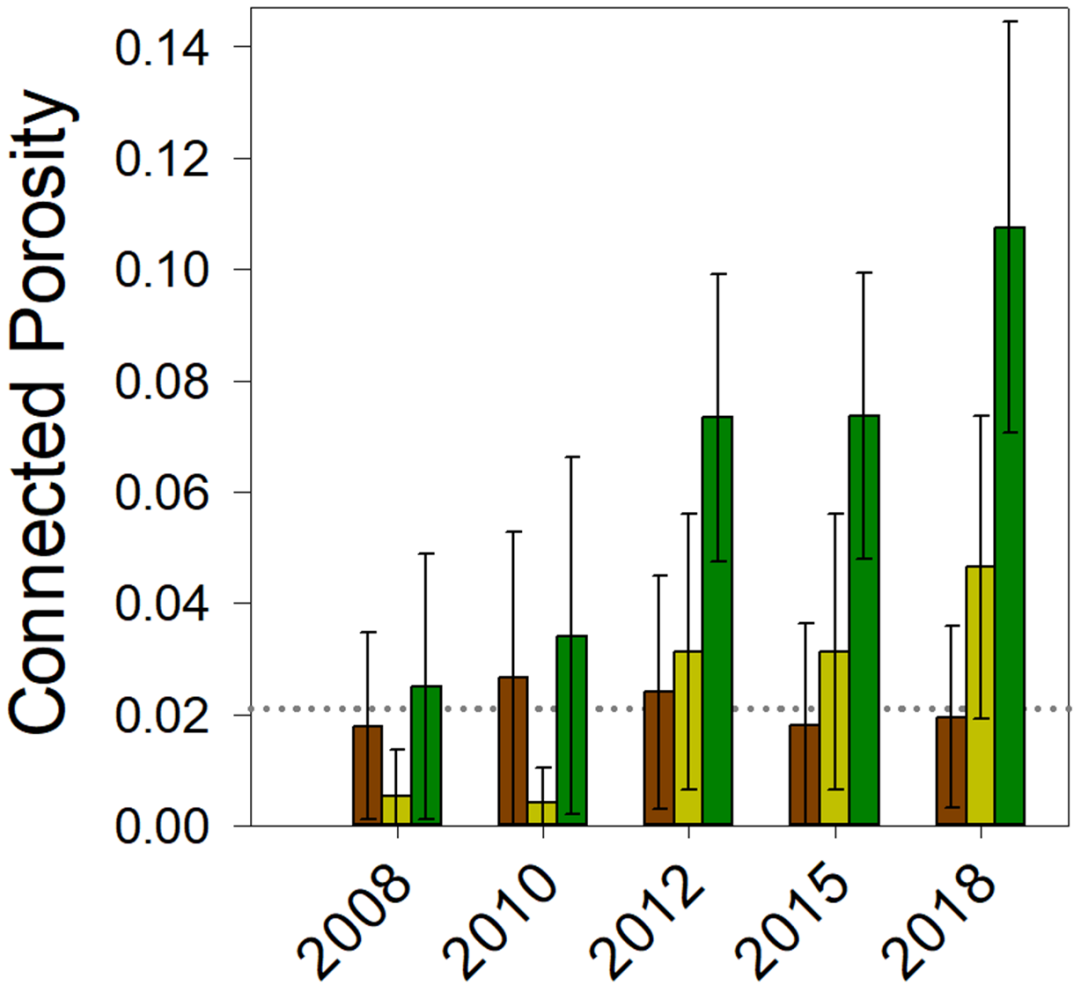

740

741 **Figure 4. Grassland soil generates connected pore space more rapidly than arable soil.**
742 Degraded soil (managed as bare fallow since 1959) developed greater connected micro-porosity
743 following conversion in 2007 to grassland than bare fallow soil converted to arable. The mean and
744 standard error of the mean of connected porosity measured in soil aggregates collected from soil
745 managed continuously as bare fallow (brown), soil converted to arable management (dark yellow)
746 and soil converted to grassland (green) over the ten years following conversion are shown. The
747 dotted line marks the mean connected porosity of continuously managed bare fallow soil over the
748 entire ten-year period.

749

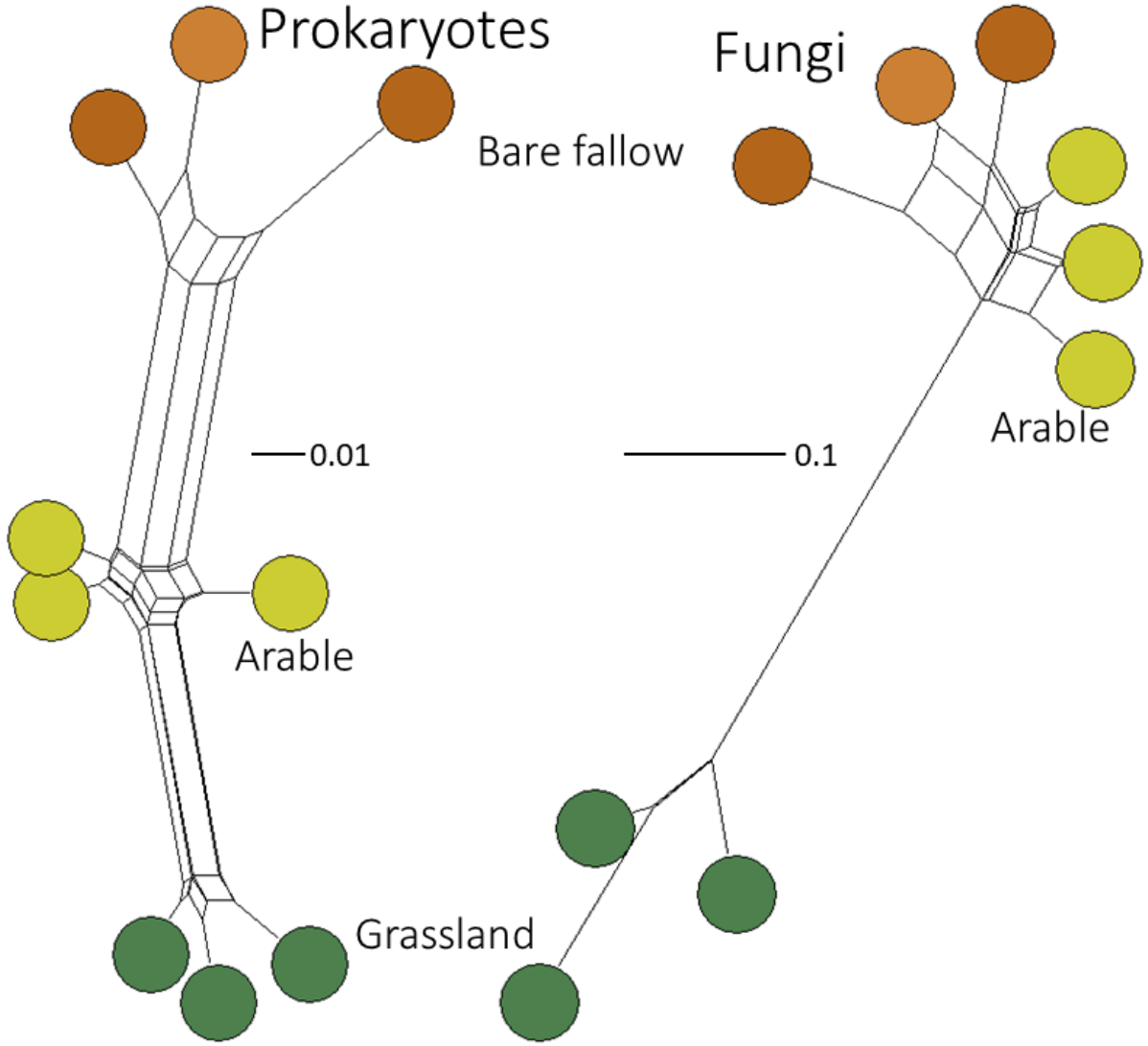

750

751 **Figure 5. Comparison of grassland, arable and bare fallowed soil microbial community *β*-**
752 **diversity.** Neighbour-Net networks of prokaryotic and fungal community profiles from the three
753 soil management types based on weighted UniFrac distance.

754

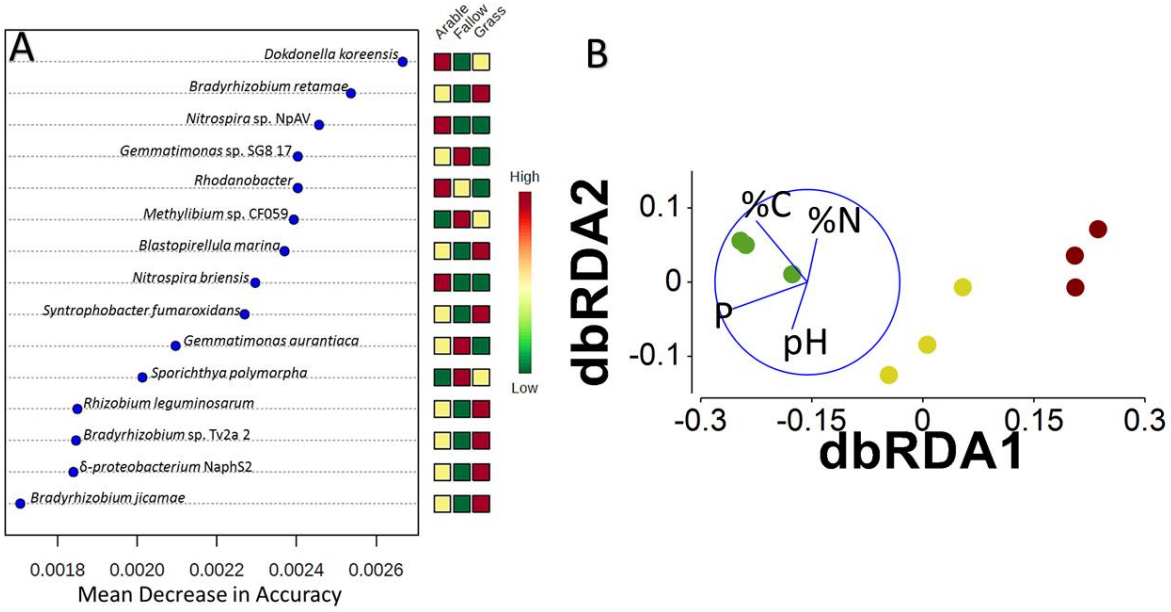

Figure 6. Taxonomy-based community responses to land management. A – Predictive modelling using a supervised Random Forest algorithm identified 15 OTUs that were most discriminatory between the different soils, based upon the mean decrease in model accuracy of a leave-one-out cross-validation procedure. **B** – Management-conditional dbRDA of chemical and physical edaphic factors and 16S rRNA-based phylogenetic assessment of microbiomes associated with the Highfield Ley-Arable experiment based upon Kantorovich-Rubinstein distances calculated from placement of homologous metagenome reads on the 16S rRNA reference phylogenetic tree. Data points represent individual replicate plots of Grassland (green), Arable (yellow) and Bare Fallow (brown) soils. Environmental factors (pH, extractable P, % organic C and % organic N) were selected by distLM as the most parsimonious combination of variables to model the multivariate data and are represented as vectors, increasing in the direction of the vector: vector length indicates the degree of partial correlation of each environmental variable with the dbRDA axes. The circle has an arbitrary origin and radius of $r = 1$. The corresponding unconstrained PCoA ordination is shown in Fig. S4. See text for a detailed description of the analysis.

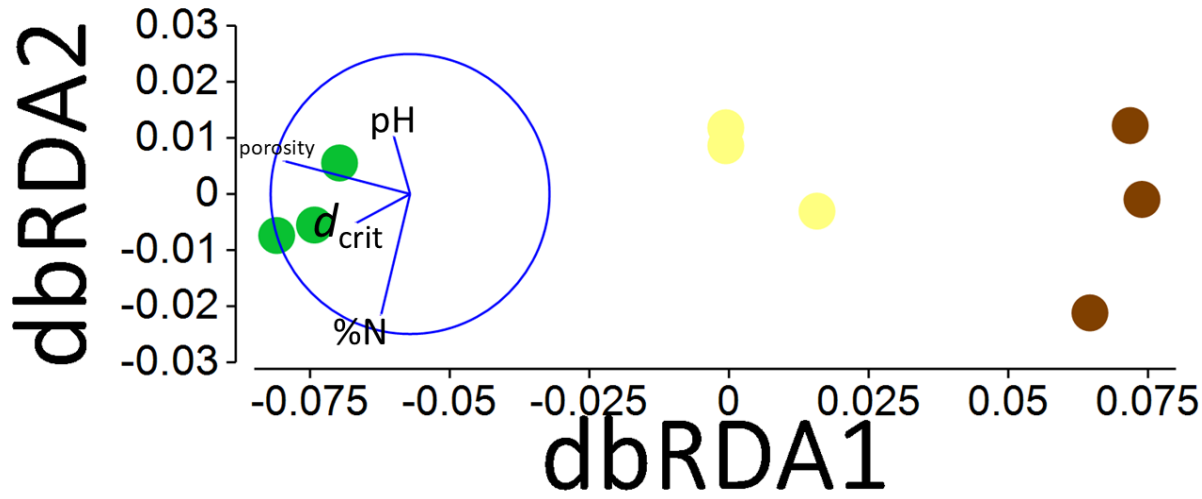

Figure 7. Function-based community responses to land management. Management-conditional dbRDA of chemical and physical edaphic factors and function-based assessment of genes associated with the Highfield Ley-Arable experiment. Square-root transformed KEGG ortholog abundances were used to calculate Hellinger distances between the nine samples. Data points represent individual replicate plots of Grassland (green), Arable (yellow) and Bare Fallow (brown) soils. Environmental factors (pH, % organic N, porosity and d_{crit}) were selected by distLM as the most parsimonious combination of variables to model the multivariate data and are represented as vectors, increasing in the direction of the vector: vector length indicates the degree of partial correlation of each environmental variable with the dbRDA axes. The circle has an arbitrary origin and radius of $r = 1$. The corresponding unconstrained PCoA ordination is shown in Fig. S5. See text for a detailed description of the analysis.

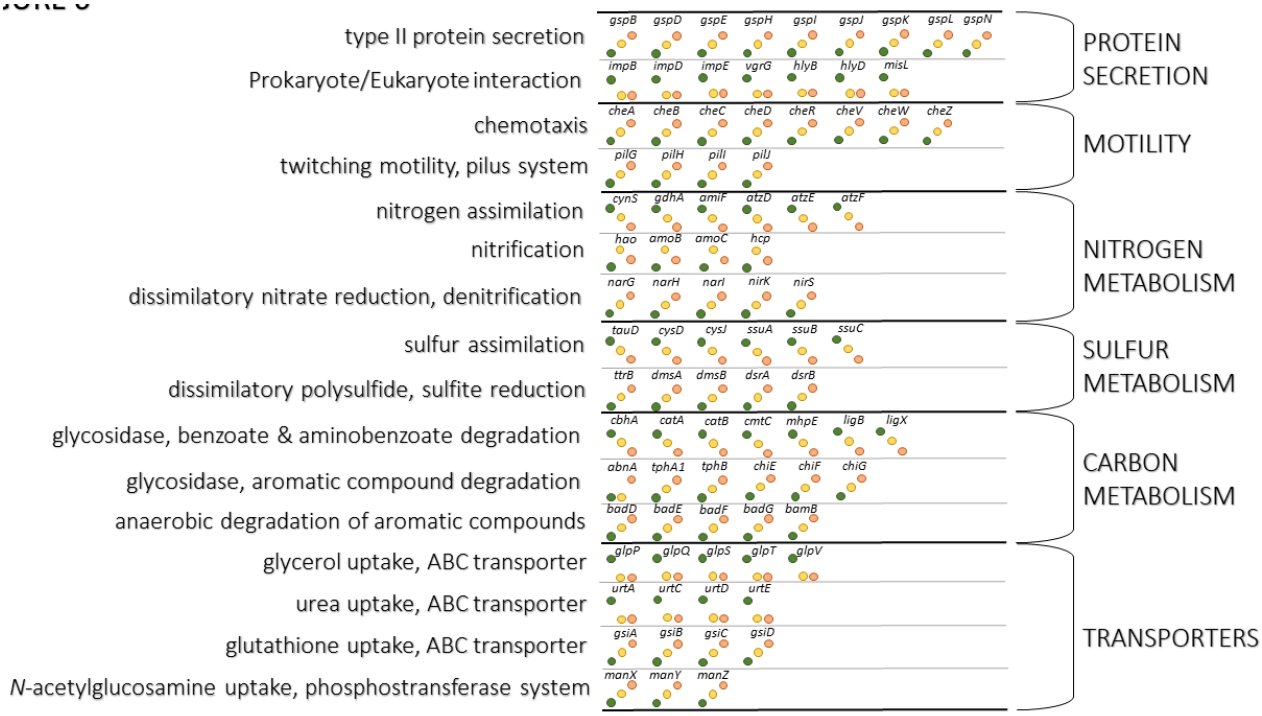

786

787 **Figure 8. Schematic representation of the relative abundance of genes for which significant**
788 **differences between the soil treatments was determined.** The central column indicates the
789 general trend in relative abundance for genes grouped according to specific functions, Grassland
790 gene abundance is represented as green points, Arable gene abundance as yellow points and Bare
791 Fallow gene abundance as brown points: each specific function is described in the left-hand
792 column; specific functions are organized into higher-level KEGG ontologies, shown in the right-
793 hand column. Absolute abundances for each gene and associated *p*- and *q*-values are shown in
794 Figs. S6 – S11.

795

	Porosity / %	Permeability / mm^2	Connectivity / μm^{-3}	Surface Density / $\mu m^2\ \mu m^{-3}$	d_{crit} / µm	Pore Neck Size / µm
Grassland (*n* = 14)	31.1 ± 1.18	1.13 ± 0.310	-0.206 ± 0.025	0.088 ± 0.003	9.74 ± 0.37	11.19 ± 0.34
Arable (*n* = 14)	23.4 ± 1.22	0.62 ± 0.154	-0.236 ± 0.033	0.092 ± 0.004	7.17 ± 0.26	8.79 ± 0.48
Bare Fallow (*n* = 9)	15.0 ± 2.21	0.55 ± 0.339	-0.018 ± 0.080	0.059 ± 0.010	3.10 ± 0.76	4.72 ± 0.95

Table 1. Topology-related parameters derived from binary images generated from X-ray Computed Tomography of aggregates from Highfield soils. The mean and standard error of each parameter is shown.

	pH (H_2O) / $-\log(g[H^+]L^{-1})$	Organic Carbon / mg g^{-1} soil	Total Nitrogen / µg g^{-1} soil	NaOH-EDTA extractable Phosphorus / µg g^{-1} soil
Grassland	6.2 ± 0.13	3.72 ± 0.44	340 ± 39.0	661.7 ± 31.3
Arable	5.8 ± 0.11	1.85 ± 0.06	190 ± 5.08	517.0 ± 12.6
Bare Fallow	5.3 ± 0.19	1.07 ± 0.10	110 ± 6.71	235.0 ± 3.8

Table 2. Summary of physical and chemical data of Highfield Ley-Arable experiment soils. The mean and standard error of the mean are shown (*n* = 3).

Supplementary Figures

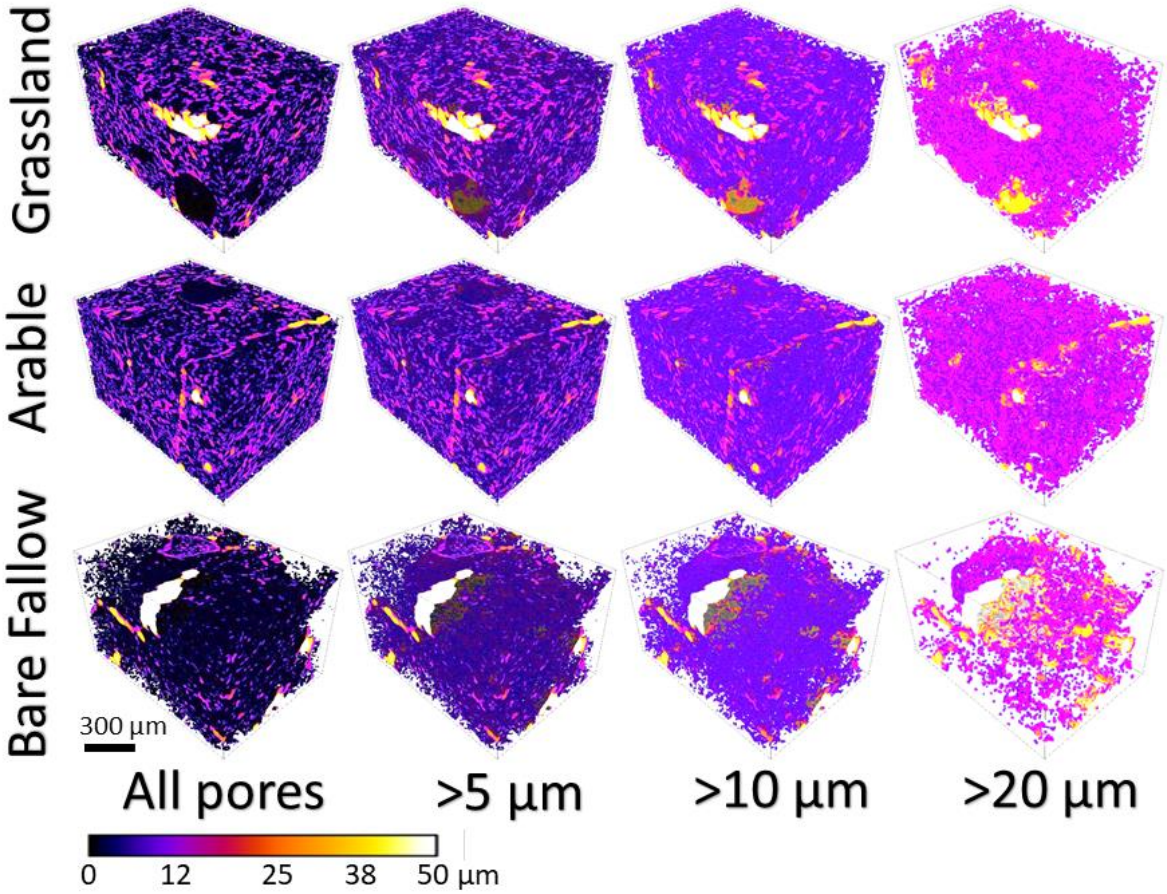

Figure S1. Three-dimensional representation of soil porosity in Highfield soils. Soil structures were determined from high-resolution (1.5 µm) X-ray Computed Tomography of aggregates (<2 mm) collected from long-term grassland, arable and bare fallowed soils. The images are pseudo-coloured to reflect the ranges of pore throat diameters present in each soil (scale shown below images) and are shown at increasingly larger pore throat diameter cut-offs for ease of discrimination. Each representation is of a typical aggregate structure collected from each soil.

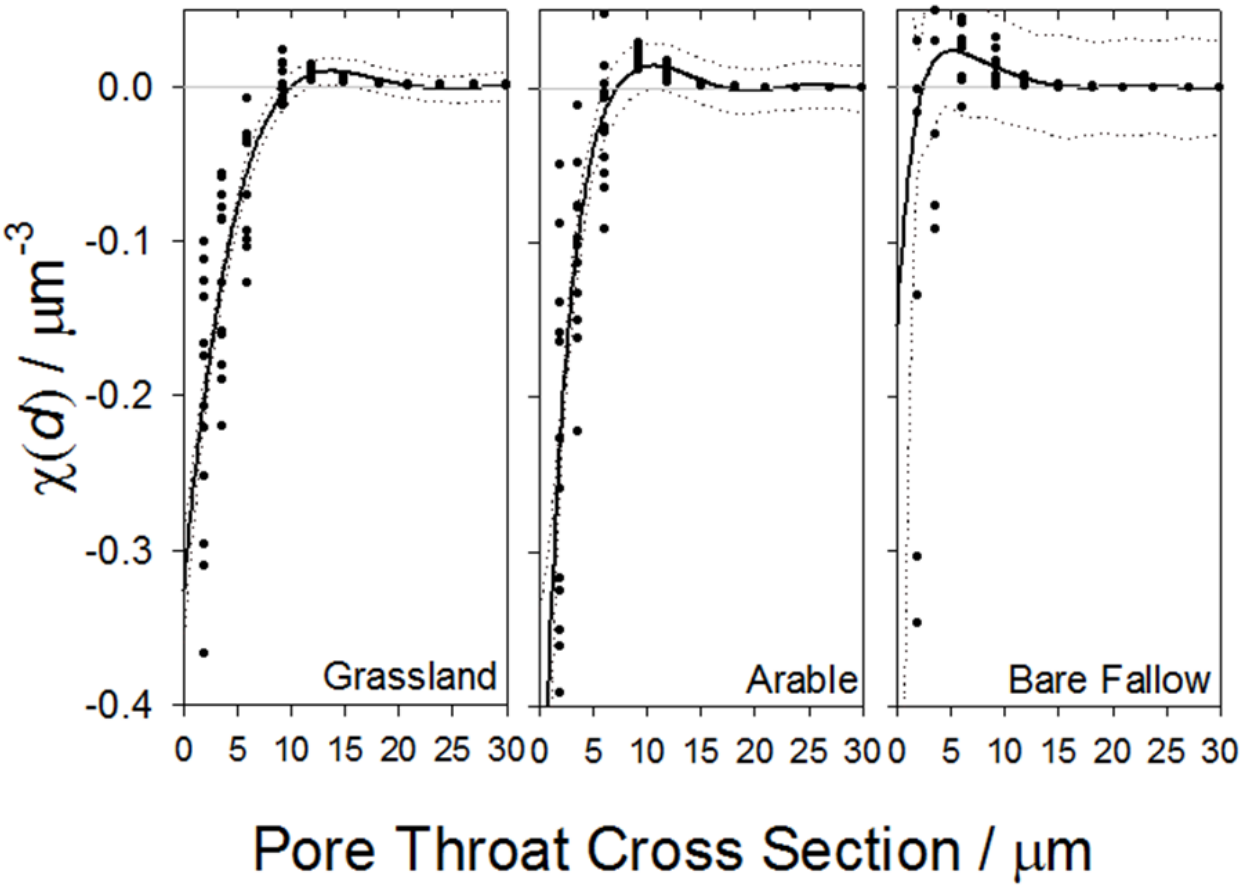

Figure S2. Euler connectivity function curves for Highfield soils generated from high-resolution (1.5 µm) X-ray Computed Tomography. Each curve presents the connectivity within and between different pore size classes. For connected pores, $\chi(d)$ takes negative values and unconnected pores positive values. The pore diameter where $\chi(d) = 0$ was estimated by fitting a polynomial to the combined data from three representative aggregates for each soil. This value, designated d_{crit}, was used as a descriptor of pore connectivity to establish the relationship between soil physical structure and differences in taxonomy and function established from metagenomics. For each soil, the solid line represents the polynomial fit to the combined data, the dashed curves represent the upper and lower 95% confidence intervals of the fit.

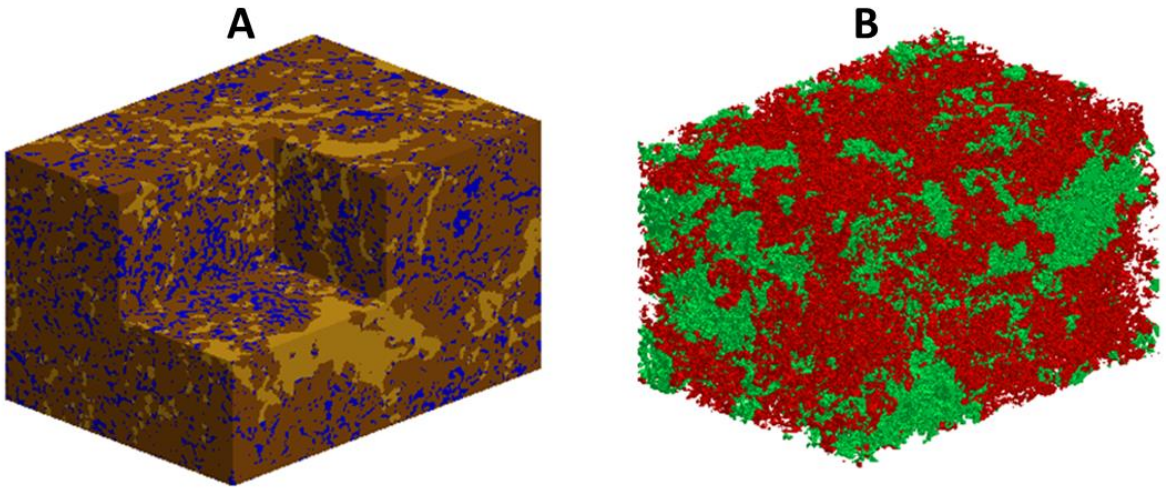

Figure S3. Water distribution and anoxic pore space within soils. A - An illustrative example showing the distribution of water (blue), air (yellow) and soil particles (brown) at saturation of 55% calculated using the proposed method. **B** - Location of anoxic (green) and aerobic (red) areas calculated from the pore-scale simulation after the system reaches steady state for $k' = 0.005$

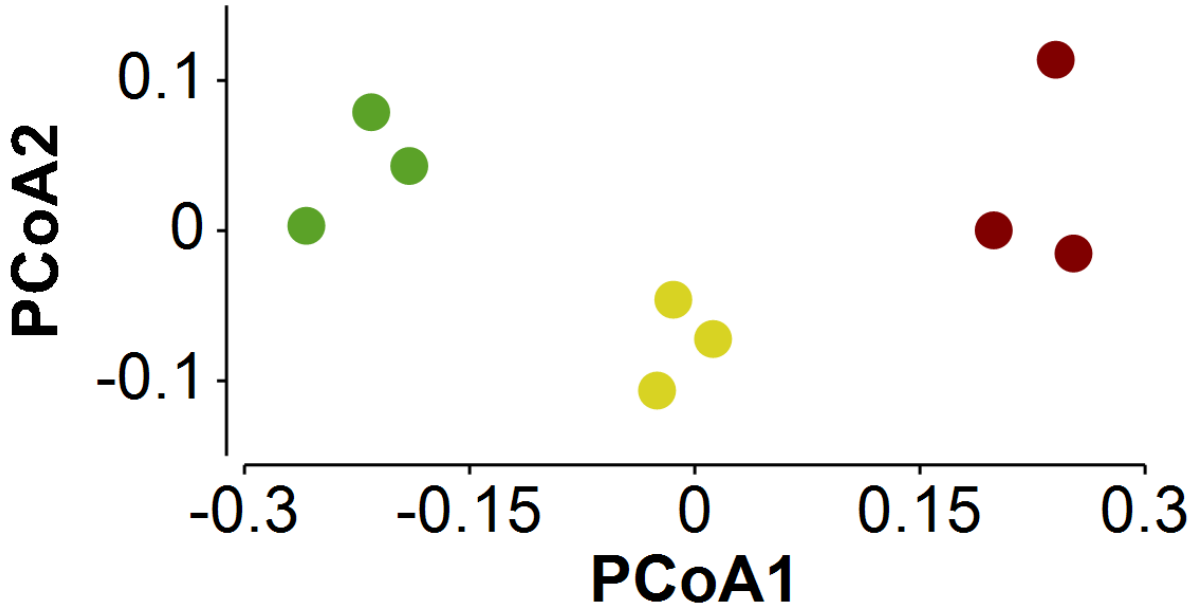

836

837 **Figure S4. Taxonomy-based comparison of community structure in Highfield soils.** Principal
838 coordinates analysis (PCoA) using weighted UniFrac distance metrics indicates clear separation
839 between the community structures in Grassland (green), Arable (yellow) and Bare fallow (brown)
840 soils. PCoA axis 1 accounted for 79.0% of total variability (eigenvalue = 0.312) and PCoA axis 2
841 for 10.1% of total variability (eigenvalue = 0.040).

842

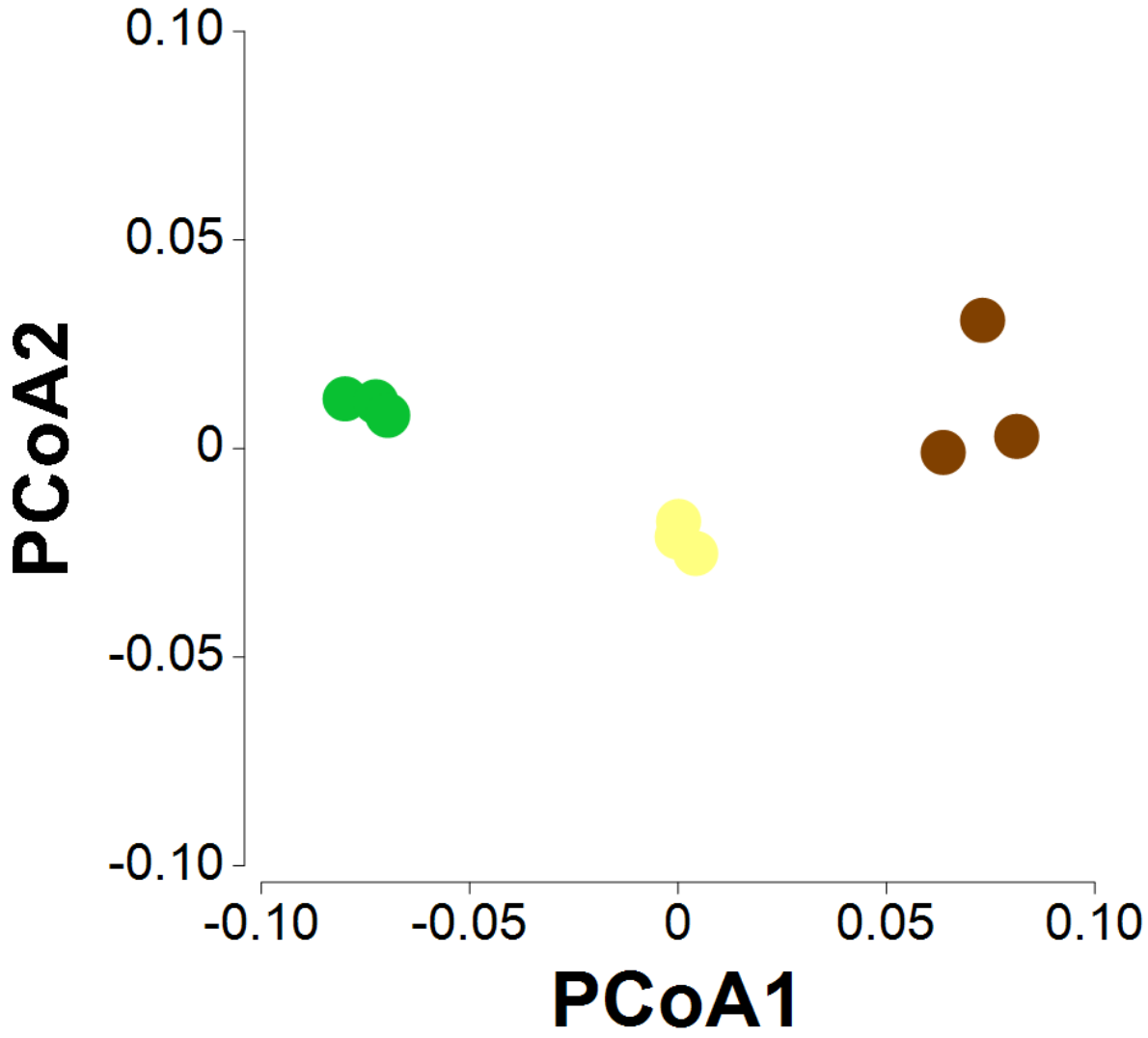

Figure S5. Function-based comparison of communities in Highfield soils. Principal coordinates analysis (PCoA) of KEGG ortholog abundance using Hellinger distance metrics indicates clear separation between microbiome function in Grassland (green), Arable (yellow) and Bare fallow (brown) soils. PCoA axis 1 accounted for 84.5% of total variability (eigenvalue 0.032) and PCoA axis 2 for 6.9% of total variability (eigenvalue 0.003).

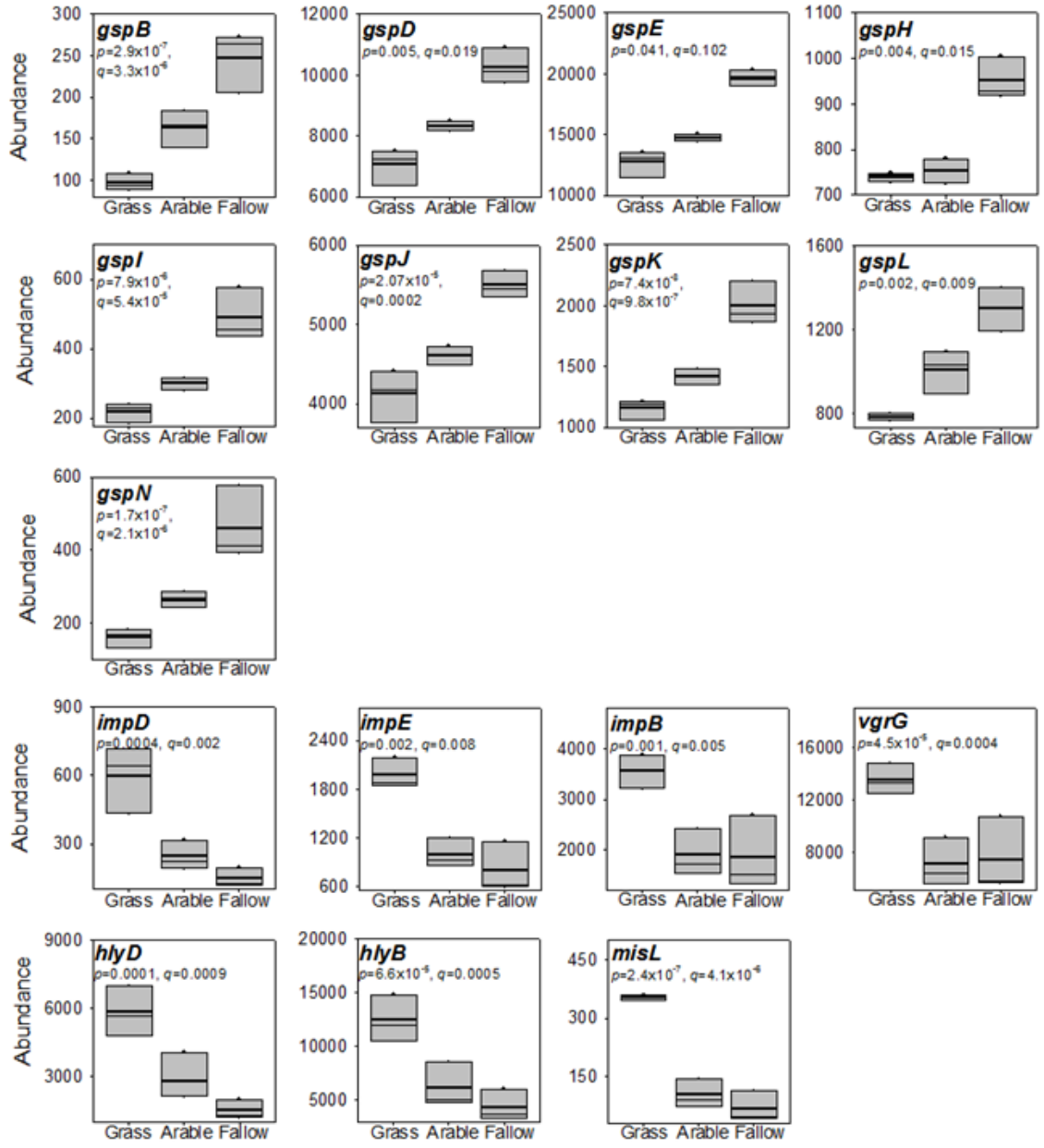

Figure S6. Genes associated with protein secretion in bacteria are more abundant in Bare fallow soil. Box plot of abundance for genes associated with the Type II Secretion System (*gspB – N*), the Type VI Secretion System (*impDEB* and *vgrG*), the Type I Secretion System (*hlyD*, *hlyB*) and the Type V Secretion System (*misL*) under different land managements. Box plot shows the mean (bold line) and median (light line) abundance together with the 5th and 95th percentiles. The significance (*p*) and positive false discovery rate (*q*) of the difference in abundance between the three treatments are shown.

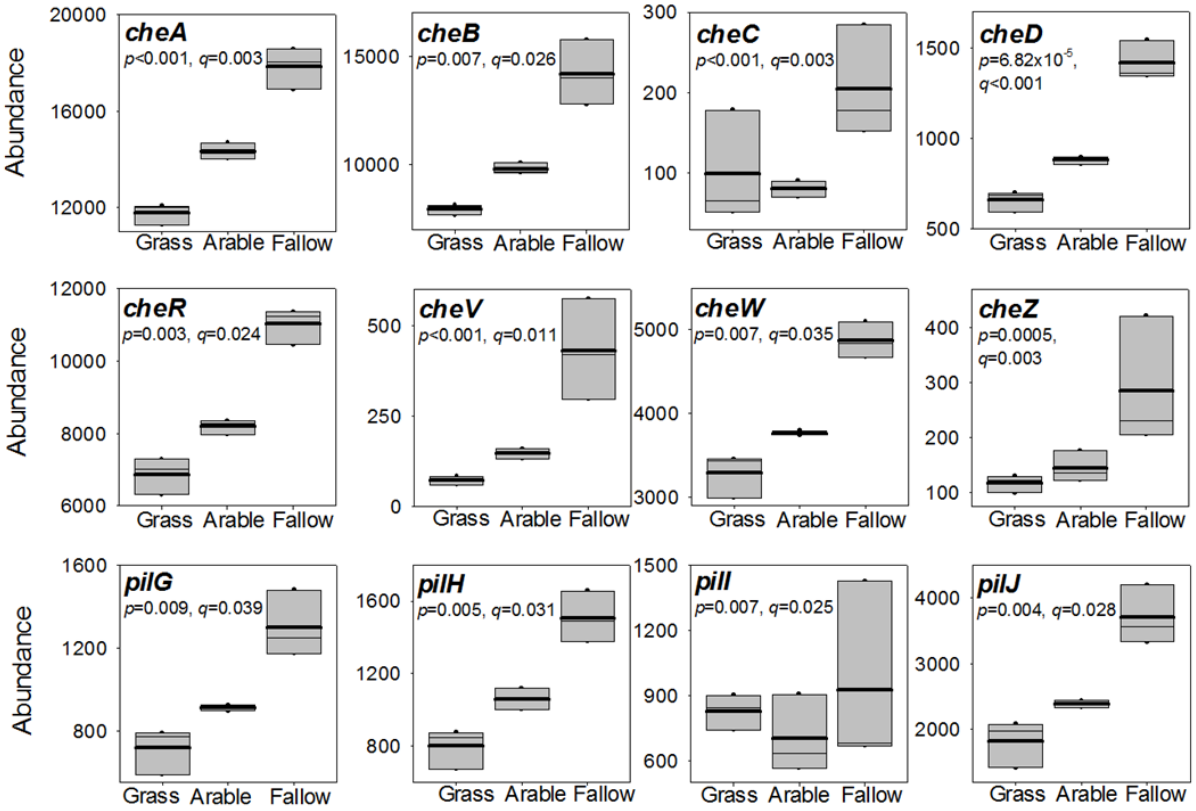

859

860 **Fig. S7. Genes associated with chemotaxis and motility in bacteria are more abundant in Bare**
861 **fallow soil**. Box plot of abundance for genes associated with chemotaxis (*cheA – Z*), type IV pili
862 synthesis (*pilG – J*) under different land managements. Box plot shows the mean (bold line) and
863 median (light line) abundance together with the 5th and 95th percentiles. The significance (*p*) and
864 positive false discovery rate (*q*) of the difference in abundance between the three treatments are
865 shown.

866

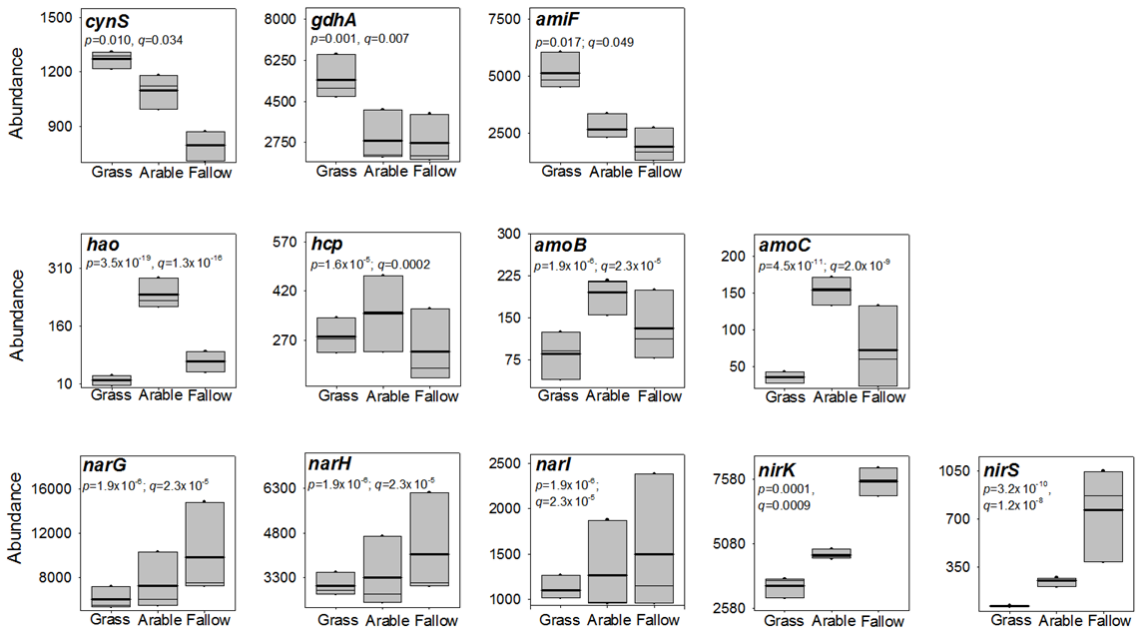

867

868 **Fig. S8. Genes associated with nitrogen metabolism show land-use specific responses.** Box plot
869 of abundance for genes associated with cyanate lyase (*cynS*), glutamate dehydrogenase (*gdhA*), the
870 oligopeptide ABC transporter, ATP-binding protein (*amiF*), hydroxylamine dehydrogenase (*hao*),
871 hydroxylamine reductase (*hcp*), the methane/ammonia monooxygenase subunits B and C (*amoB*,
872 *amoC*), nitrate reductase/nitrite oxidoreductase alpha- beta- and gamma-subunits (*narGHI*), and
873 nitrite reductase (*nirK* and *nirS*). Box plot shows the mean (bold line) and median (light line)
874 abundance together with the 5th and 95th percentiles. The significance (*p*) and positive false
875 discovery rate (*q*) of the difference in abundance between the three treatments are shown.

876

877

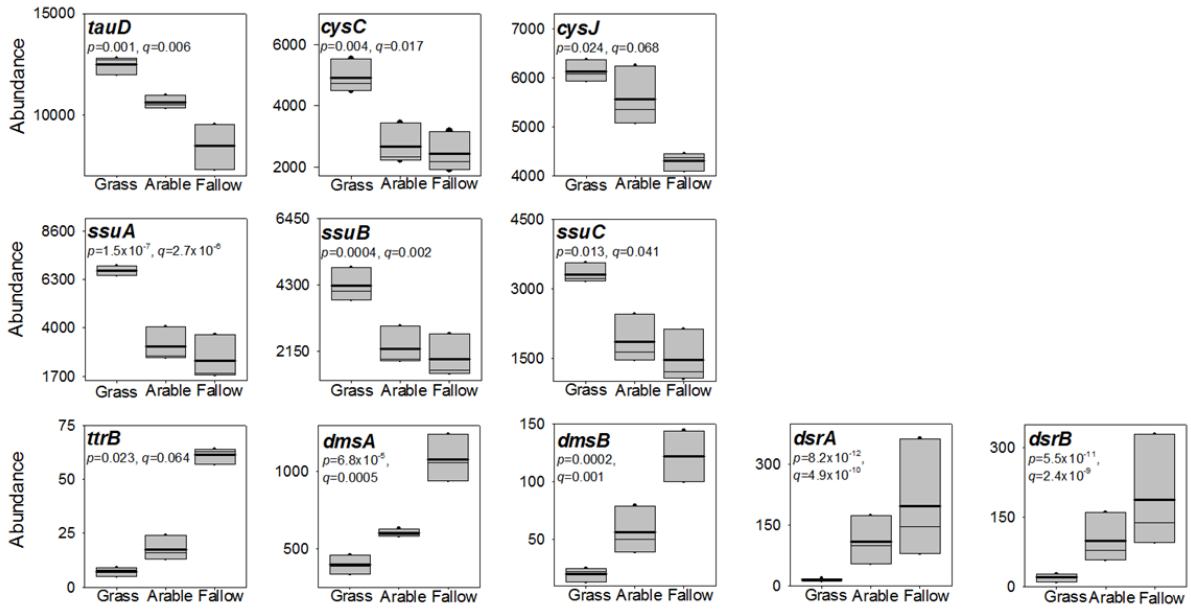

878

879 **Figure S9. Genes associated with sulfur metabolism show land-use specific responses.** Box plot
880 of abundance for genes associated with an α-ketoglutarate-dependent dioxygenase which degrades
881 2-aminoethansulfonic acid (*tauD*), adenylylsulfate kinase (*cysC*), sulfite reductase flavoprotein
882 alpha-component (*cysJ*), sulfonate transport system (*ssuABC*), tetrathionate reductase (*ttrB*),
883 dimethyl sulfoxide reductase (*dmsAB*), and dissimilatory sulfite reductase alpha- and beta-subunits
884 (*dsrAB*). Box plot shows the mean (bold line) and median (light line) abundance together with the
885 5th and 95th percentiles. The significance (*p*) and positive false discovery rate (*q*) of the difference
886 in abundance between the three treatments are shown.

887

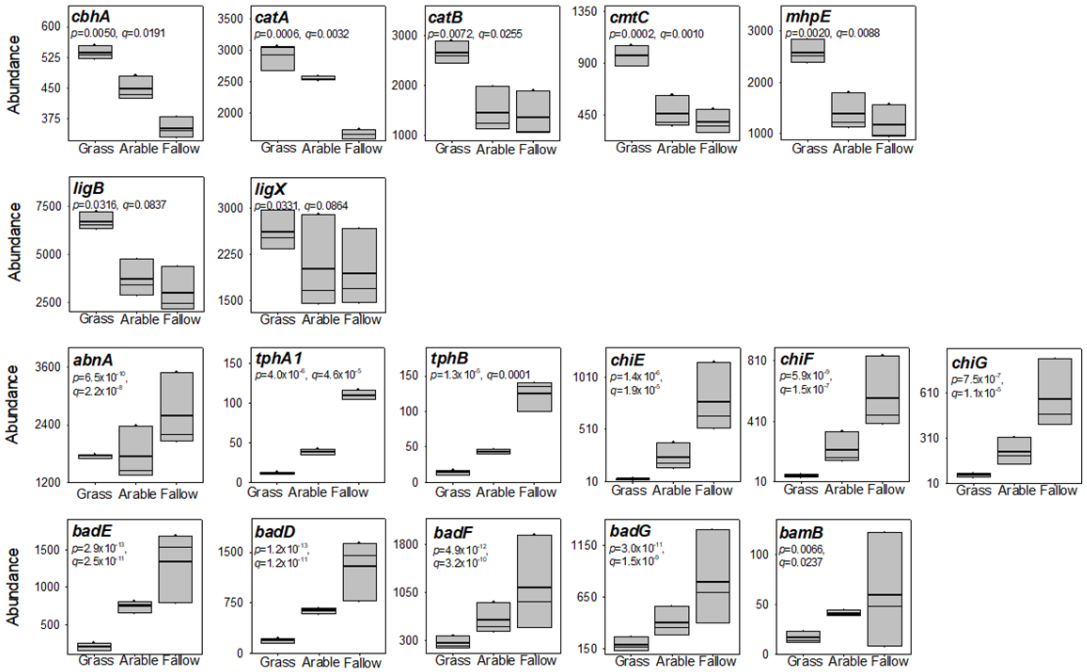

888

889 **Figure S10. Genes associated with carbohydrate metabolism show land-use specific responses.**
890 Box plot of abundance for genes associated with cellulose 1,4-β-cellobiosidase (*cbhA*), catechol 1,2-
891 dioxygenase (*catA*), muconate cycloisomerase (*catB*), 2,3-dihydroxy-*p*-cumate/2,3-
892 dihydroxybenzoate-3,4-dioxygenase (*cmtC*), 4-hydroxy-2-oxovalerate aldolase (*mhpE*),
893 protocatechuate 4,5-dioxygenase (*ligB*), 5,5'-dehydrodivanillate *O*-demethylase (*ligX*), arabinan
894 endo-1,5-alpha-*L*-arabinosidase (*abnA*), terephthalate 1,2-dioxygenase reductase (*tphA1*), 1,2-
895 dihydroxy-3,5-cyclohexadiene-1,4-dicarboxylate dehydrogenase (*tphB*), benzoyl-CoA reductase
896 subunits A, B, C and D (*badFEDG*) and benzoyl-CoA reductase subunit (*bamB*). Box plot shows
897 the mean (bold line) and median (light line) abundance together with the 5th and 95th percentiles.
898 The significance (*p*) and positive false discovery rate (*q*) of the difference in abundance between
899 the three treatments are shown.

900

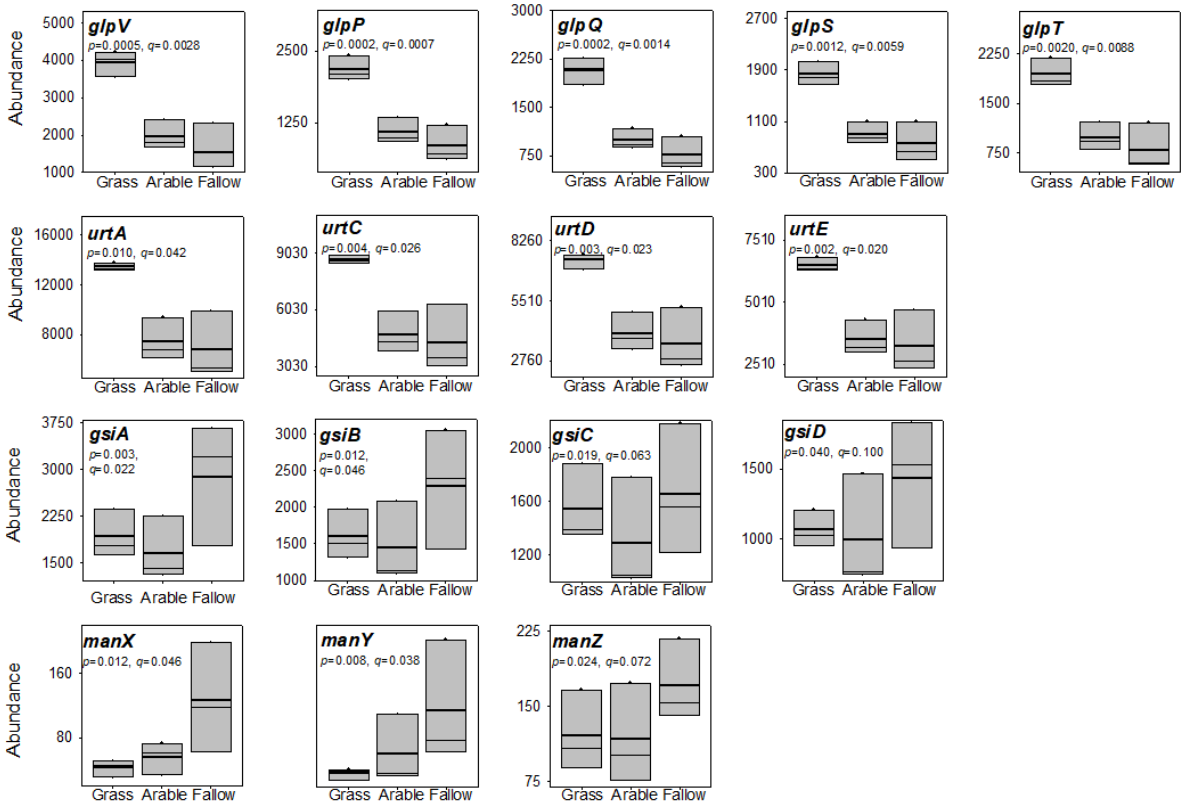

Fig. S11. Genes associated with solute transport show land-use specific responses. Box plot of abundance for genes associated with transport of glycerol (*glpVPQST*), urea (*urtACDE*), glutathione (*gsiABCD*) and glucose, mannose, glucosamine and *N*-acetylglucosamine transport (*manXYZ*). Box plot shows the mean (bold line) and median (light line) abundance together with the 5th and 95th percentiles. The significance (*p*) and positive false discovery rate (*q*) of the difference in abundance between the three treatments are shown.